UNIVERSITA' DEGLI STUDI DELL'INSUBRIA

DOTTORATO DI RICERCA IN SCIENZE DELLA VITA E BIOTECNOLOGIE
XXXVII CICLO

Innovative diagnostic and therapy pathway for patient with maculopathy, from genetics and biomarkers to telemedicine

Percorso diagnostico terapeutico innovativo per pazienti con maculopatia, dalla genetica e i biomarkers alla telemedicina

Docente guida: Prof. Simone Donati

Tesi di Dottorato di:
Dott. Elias Premi
Matricola 75055

Dipartimento Biotecnologie e Scienze della Vita – Università degli Studi dell'Insubria
Anno Accademico 2023/2024

General Introduction

Macular diseases represent one of the leading causes of visual impairment in industrialized countries and constitute an area of growing clinical and scientific relevance. Conditions such as macular edema secondary to retinal vein occlusion (RVO), diabetic retinopathy, and degenerative maculopathies share complex pathophysiological mechanisms characterized by the interaction between vascular damage, neuronal alterations, and glial dysfunction. In this context, Müller cells play a pivotal role in maintaining retinal homeostasis by regulating fluid balance, oxidative metabolism, and blood–retinal barrier integrity.

At the same time, the advent of multimodal imaging—particularly high-resolution optical coherence tomography (OCT)—has enabled the identification of structural biomarkers associated with functional prognosis in vascular macular diseases. Despite significant therapeutic advances, especially with anti-VEGF agents, a substantial proportion of patients exhibit incomplete response or persistent edema, suggesting that the underlying mechanisms are not exclusively vascular but also involve the neuroglial compartment. Furthermore, the increasing development of telemedicine introduces new perspectives for the remote functional monitoring of patients affected by chronic retinal diseases.

In light of these considerations, this thesis aims to explore, in an integrated manner, the molecular, structural, and functional determinants of retinal response in macular diseases. The work is organized into three complementary parts.

Chapter I – Molecular Modulation of Müller Cells After Subthreshold Laser Treatment

The first part focuses on the transcriptional response of Müller cells following subthreshold laser stimulation. This treatment strategy is conceived as a bio-stimulatory rather than photocoagulative approach, designed to modulate cellular mechanisms without inducing visible thermal damage. Through gene expression analysis, the study investigates the modulation of pathways involved in fluid homeostasis, extracellular matrix remodeling, and oxidative stress regulation, with particular attention to genes related to apoptosis and cell death. The objective is to clarify whether subthreshold laser acts through controlled activation of Müller cells, enhancing their homeostatic function without triggering reactive gliosis or neurodegenerative processes.

Chapter II – OCT Biomarkers in Macular Edema Secondary to Retinal Vein Occlusion

The second part examines the prognostic value of structural OCT biomarkers in macular edema secondary to RVO. Specifically, the study evaluates the association between the integrity of outer retinal bands—namely the external limiting membrane and the ellipsoid zone—, the architecture of the Müller cell cone, and the evolution of edema following anti-VEGF therapy. In addition, the clinical significance of foveal eversion, described as a potential marker of persistent edema, is assessed. The aim is to determine to what extent structural preservation of the neuroglial compartment influences anatomical and functional recovery, helping to explain the discrepancy sometimes observed between reduction in retinal thickness and improvement in visual acuity.

Chapter III – Validation of Digital Functional Testing in Macular Diseases

The third part addresses the evaluation of digital tools for functional monitoring in macular diseases. In particular, a smartphone-based visual acuity test and a digital Amsler grid are analyzed and compared with standard in-clinic assessments. The objective is to determine the reliability, reproducibility, and

clinical correlation of these tools, and to assess their potential integration into telemonitoring pathways for patients with chronic macular conditions.

Translational rationale

Although the three studies included in this thesis address different methodological levels, they are conceived as consecutive and complementary steps within the same translational framework.

The first part investigates the molecular response of Müller glial cells to subthreshold laser stimulation, aiming to identify whether a non-destructive therapeutic stimulus can induce transcriptional changes potentially related to cellular homeostasis, ion transport, extracellular matrix remodeling, oxidative stress regulation, and preservation of non-cytotoxic cellular adaptation. This molecular layer provides the biological foundation for considering Müller cells not only as passive structural elements of the retina, but as dynamic regulators of tissue response.

The second part translates this cellular concept into clinical imaging by assessing OCT biomarkers that may indirectly reflect neuroglial integrity in macular edema secondary to retinal vein occlusion. In this context, the Müller cell cone, outer retinal band integrity, foveal architecture, and edema persistence are interpreted as structural manifestations of the balance between retinal injury and reparative capacity. While OCT cannot directly visualize molecular pathways, it provides a clinically accessible surrogate of retinal organization, allowing the investigation of whether preservation of neuroglial architecture is associated with anatomical recovery after anti-VEGF therapy.

The third part extends this translational pathway toward functional assessment and telemedicine. If molecular and structural biomarkers contribute to defining disease mechanisms and anatomical prognosis, digital functional testing may support longitudinal monitoring outside the conventional hospital setting. Smartphone-based visual acuity assessment and digital Amsler grid testing

therefore represent a pragmatic clinical extension of the same model: moving from cellular mechanisms to imaging biomarkers, and finally to scalable patient-centered monitoring tools.

Thus, the thesis follows a progressive translational sequence: first, the biological modulation of Müller cells is explored at the transcriptomic level; second, Müller cell-related structural biomarkers are evaluated using OCT in a clinical vascular macular disease model; third, digital tools are validated to support functional monitoring in patients with macular disease. This integration supports the broader hypothesis that personalized management of macular diseases requires the combined interpretation of molecular mechanisms, retinal microstructure, and functional evolution.

Chapter 1

Subthreshold laser treatment in a MIO-M1 in vitro experimental model

Introduction

Subthreshold laser therapy, particularly in its micro pulse modality, has emerged over the past two decades as a therapeutic strategy for macular edema that differs fundamentally from conventional photocoagulation. Unlike continuous-wave laser photocoagulation, which induces visible retinal burns and tissue necrosis, subthreshold/micro pulse laser delivers energy in short, repetitive pulses with intervening cooling periods, thereby avoiding overt retinal damage while preserving photoreceptors and inner retinal architecture. Clinically, this approach has demonstrated efficacy in diabetic macular edema (DME) and other exudative maculopathies, often with a favorable safety profile and minimal structural disruption on retinal imaging, especially using optical coherence tomography (OCT).

From a mechanistic standpoint, subthreshold laser is widely conceptualized as a form of “cellular photo stimulation” rather than tissue ablation. Experimental evidence indicates that sublethal photothermal stimulation can induce heat-shock protein (HSP) pathways and cytoprotective responses in retinal cells, particularly within the retinal pigment epithelium (RPE).
In vitro models have shown that micro pulse laser exposure upregulates stress-response genes, including Hsp70, supporting the hypothesis that laser-induced, nonlethal stress triggers adaptive and homeostatic signaling cascades rather than cell death[1] These findings have provided a molecular framework for interpreting the clinical benefits of subthreshold laser as secondary to stress-mediated cellular reprogramming.

More recently, transcriptomic approaches have directly confirmed that subthreshold micro pulse laser can induce measurable gene-expression changes in retinal support cells[2]. In a human pluripotent stem cell–derived RPE model, RNA-sequencing demonstrated that subthreshold micro pulse laser elicits a distinct differential expression profile compared to continuous-wave photocoagulation, with modulation of genes involved in stress responses and cellular homeostasis[3]. Importantly, the number and magnitude of differentially

expressed genes were lower than those induced by continuous-wave laser, consistent with a non-destructive, regulatory mode of action. These data provide robust evidence that subthreshold laser can reprogram retinal support-cell transcription without inducing widespread cytotoxicity.

Despite this progress, most molecular investigations have focused on the RPE, leaving the contribution of Müller glial cells largely unexplored. This represents a critical limitation, given that Müller cells are the principal macroglial cells of the retina and play a central role in retinal homeostasis, especially considering the internal blood retinal barrier (iBRB). They regulate extracellular potassium buffering, water distribution, metabolic support, neurotransmitter recycling, and structural stabilization of the neurovascular unit. In the context of macular edema, Müller cells are particularly relevant because they participate in ionic and osmotic regulation and contribute to inner iBRB integrity through cross-talk with endothelial cells and pericytes[4].

Beyond their well-established metabolic and homeostatic functions, Müller glial cells play a critical and often underappreciated role in retinal optics. Spanning the entire thickness of the retina—from the inner limiting membrane (ILM) to the outer limiting membrane (OLM)—Müller cells are uniquely positioned to influence the propagation of light through the multilayered neural tissue before it reaches the photoreceptor outer segments. In vertebrate retinas, incident light must traverse multiple neuronal and synaptic layers prior to phototransduction, creating the potential for scattering and optical degradation. The elongated, radially oriented morphology and specialized intracellular architecture of Müller cells have been shown to mitigate this problem by functioning as biological optical fibers.

Experimental works combining confocal microscopy, optical modeling, and micro-optical measurements demonstrated that Müller cells guide light through the retina with properties analogous to optical fibers[5,6]. These studies showed that isolated Müller cells transmit light preferentially along their longitudinal axis with minimal lateral dispersion, effectively channeling photons toward photoreceptor inner and outer segments. The high refractive index of Müller

cell cytoplasm relative to the surrounding extracellular matrix and neuronal tissue creates conditions favorable for total internal reflection, a fundamental principle of fiber-optic waveguiding. As a result, Müller cells reduce intraretinal scattering and enhance the efficiency and directionality of photon delivery to photoreceptors.

Subsequent investigations further refined this concept, demonstrating that the funnel-shaped endfeet of Müller cells at the ILM are particularly suited to collect incident light and direct it into the narrower central shaft of the cell, optimizing coupling efficiency between incoming photons and the waveguiding structure[7]. This optical specialization appears to be evolutionarily conserved and is especially relevant in species with inverted retinas, such as mammals, where light must pass through neuronal layers before reaching photoreceptors[8].

Importantly, the optical function of Müller cells is tightly integrated with their structural and cytoskeletal organization. The alignment of intermediate filaments and the spatial distribution of organelles contribute to minimizing optical inhomogeneities that would otherwise increase scattering. Pathological conditions that induce Müller cell swelling, reactive gliosis, or cytoskeletal remodeling—such as diabetic macular edema—may therefore disrupt not only ionic and fluid homeostasis but also retinal light transmission efficiency.

Given these properties of biological fiber optics, Muller cells could also transmit laser light focused on ILM endfeet through their entire body, in which cellular nuclei reside.

Clinical biomarker studies provide indirect but compelling evidence that Müller cells may be involved in the therapeutic response to subthreshold micropulse laser. In patients with DME treated with subthreshold micropulse laser, aqueous humor analysis revealed significant modulation of glial and inflammatory biomarkers, including reductions in glial fibrillary acidic protein (GFAP) and Kir4.1, along with decreased VEGF levels[9]. Because GFAP is a canonical marker of Müller cell activation and Kir4.1 is a key component of Müller potassium homeostasis, these findings were interpreted as indicative of reduced Müller reactivity and possible restoration of glial homeostatic function following treatment. Additional clinical investigations have similarly demonstrated modulation of inflammatory and vasoactive mediators after subthreshold

micropulse laser, reinforcing the concept that this therapy alters the intraocular molecular milieu rather than producing a purely structural effect[10]

However, these human studies rely on aqueous humor protein quantification and cannot determine whether the observed changes originate directly from Müller cells, RPE, endothelial cells, or other retinal components. Likewise, RPE transcriptomic data, although mechanistically informative, do not clarify whether Müller cells undergo parallel or distinct transcriptional reprogramming in response to subthreshold laser exposure. To date, there is a paucity of studies specifically addressing Müller cell gene expression following subthreshold or micro pulse laser treatment. This absence of direct Müller transcriptomic evidence constitutes a significant gap in the current understanding of laser-induced retinal modulation and in observable clinical effects on disease linked to iBRB instability.

Given the well-established role of Müller cells in retinal fluid homeostasis and iBRB regulation, the lack of cell-specific gene-expression data represents an important unmet need. If subthreshold laser facilitates macular edema resorption clinically, a plausible mechanism could involve transcriptional modulation of Müller cell pathways governing ionic balance, osmotic gradients, inflammatory signaling, or neurovascular cross-talk. Yet, without direct molecular interrogation of Müller cells, such hypotheses remain speculative.

In this context, transcriptomic analysis of Müller cells following controlled subthreshold laser exposure provides a novel translational and necessary investigative step. By directly assessing differential gene expression in Müller cells subjected to defined laser parameters, it becomes possible to determine whether subthreshold photo stimulation induces molecular programs consistent with enhanced fluid regulation, modulation of barrier-associated signaling, or adaptive stress responses. Such data can bridge the current gap between RPE-centered transcriptomic findings, aqueous humor biomarker modulation of Müller linked protein, and the clinically observed improvement in retinal edema.

Aim of the study

The aim of the present study was to investigate, in a controlled experimental setting, the direct transcriptional effects of subthreshold green laser irradiation on Müller glial cells. Given the central role of Müller cells in retinal fluid homeostasis, ionic regulation, neurovascular unit stability, and structural support, we hypothesized that subthreshold laser exposure may induce transcriptional reprogramming of pathways involved in ion transport, cell-volume regulation, and barrier-associated signaling. Concurrently, we aimed to verify that subthreshold laser treatment did not trigger cellular death or apoptotic pathways.

To address this hypothesis, we employed an in vitro experimental model using the human Müller cell line MIO-M1, which retains key phenotypic and functional characteristics of retinal Müller glia[11].

By isolating Müller cells from the complex retinal microenvironment, this model was designed to determine whether subthreshold laser directly induces gene-expression changes consistent with enhanced fluid regulation, modulation of inflammatory or permeability-related signaling, or activation of adaptive stress-response pathways. Through this approach, the study aims to bridge the gap between clinical observations of edema resolution and the molecular mechanisms operating at the level of retinal glial cells.

Material and Methods

MIO-M1 cell line

The MIO-M1 is a Müller adherent cell line derived from the spontaneous immortalization (at least 100 divisions) retina obtained from a 68-year-old female corneal donor, 36 hours after death[11].

Cells have been cultured in Dulbecco's Modified Eagle Medium (DMEM) supplemented with 10% Fetal Bovine Serum (FBS), 1% L-Glutamine and 1% Penicillin/Streptomycin and maintained at 37°C, 5% CO_2 atmosphere.

Cell culture preparation

MIO-M1 cells were cultured as described in the previous paragraph. Upon confluence, the cells were washed twice with sterile phosphate buffer saline (PBS) and detached from the flask using trypsin-EDTA diluted in sterile PBS (1:1 ratio).

Cells were counted with a Burker chamber and plated in a 48-well at a concentration of 15000 cells/wells. Each treatment has been performed in duplicate. To be sure to have enough material for further analysis, three wells were considered for each sample.

A total of 12 wells were used for each experiment (6 for the two controls, 6 for the low-level intensity and 6 for the high-level intensity; fig. 1).

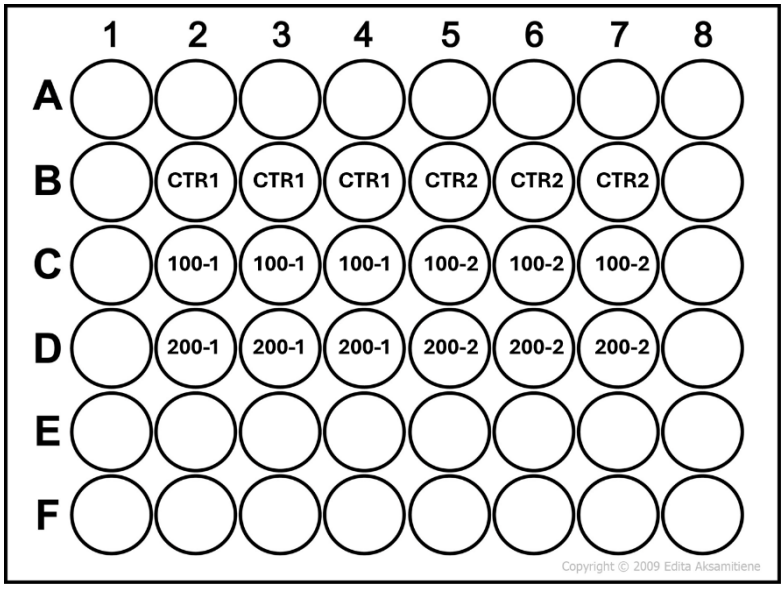

Fig. 1: schematic representation of cells treatment. We had a total of 6 samples (CTR1, CTR2, 100-1, 100-2, 200-1 and 200-2). Each sample is composed by three wells.

The treatment was conducted on the cells at four passages after thawing and generally the cells were cultured for no more than five to six passages.

Treatment

The ECHO 520nm laser (Norlase, Denmark) was installed on a home-made support, that allowed to direct the laser toward the bottom of the wells.
Two subthreshold impulse intensities were chosen: the low level 3.2 J/cm^2 corresponding to the 100mW setting used in clinics (named 100), and an higher level of 6.4 J/cm2 corresponding to the 200mW (named 200) that can be used in patients. A spot size of 200 micron and a duration of 200ms were chosen. A multiple spot square design of 5X5 of laser impulses were set to cover the entire well surface with sequential spatial treatment. The navigation was guided by a dark graph paper. After treatment, cells have been cultured for 24h or 72h and then the RNA was extracted.

Control of potential scattered laser exposure

Specific procedural precautions were adopted to minimize unintended laser exposure of adjacent wells and to reduce the risk of scattered or reflected light during treatment. The wells used for irradiation had a frosted rim, which helped limit lateral light propagation at the level of the well borders. In addition, black millimeter graph paper was placed underneath the bottom of the wells to guide spatial targeting and to reduce possible back-reflections from the support surface.

Laser delivery was performed under microscopic guidance using an inverted microscope. The laser beam was precisely focused within the selected well, and the aiming beams were carefully maintained inside the well area without colliding with the well walls. Irradiation was performed sequentially, one well at a time, and laser activation occurred only after accurate positioning of the target area. This approach was applied to both treatment conditions, thereby minimizing potential cross-exposure between control wells and wells treated at 100 mW or 200 mW.

Although no dedicated quantitative measurement of scattered light reaching adjacent wells was performed, the combination of frosted well borders, black non-reflective graph paper underneath the wells, microscopic guidance, accurate beam alignment, and avoidance of beam-wall collision was adopted to substantially reduce the possibility of relevant unintended irradiation. Therefore, transcriptomic differences between control and treated samples were considered primarily attributable to the assigned laser exposure conditions.

RNA extraction and quality control

RNA extraction was performed by pooling cells plated in the three wells of each sample, to obtain sufficient material to be analysed.

Total RNA was extracted with the Quick-RNA Miniprep Kit (Zymo Research Inc) and subsequently quantified using a NanoDrop ND 1000 spectrophotometer (Thermo Fisher Scientific), following manufacturer instructions.
RNA integrity has been checked on a 0.7% agarose gel made with TBE in DEPC water. 100ng of RNA have been mixed with a 2x RNA loading dye (New England Biolabs), heated to 65°C for 10' and loaded onto the gel. A ssRNA ladder (Fig. 2) has been prepared and loaded on the agarose gel.

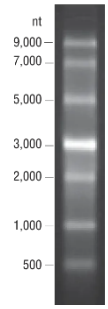

Fig. 2: ssRNA ladder.

RNA-seq

RNASeq has been performed by IGA Technologies (Udine, Italy). 120ng RNA has been diluted to a final volume of 20µl and shipped to the sequencing company. A Total RNA sequencing approach has been followed.

RNA-seq differential analysis

Paired-end reads of 150bp in length generated by RNA-seq were quality checked using fastqc v0.11.8 (Andrews 2010) and aligned to the GENCODE Homo Sapiens genome (build GRCh38/hg38) using STAR v2.7.11a[12]. Mapped reads were assigned to gene features by FeatureCounts v2.0.6[13] using as annotation file the comprehensive gene annotation on reference chromosomes (v49 GENCODE release). The generated count table was later normalized with Trimmed Means of M values (TMM) method implemented in edgeR v3.40.0[14] and lowly expressed genes were filtered out with edgeR's filterByExpr R function. Normalized read counts were transformed into $\log_2$ counts per million (CPM) values and corrected for latent sources of variation using surrogate variables estimated by the sva R package v3.46.0[15]. Differential expression was assessed using voom, lmFit, and

eBayes functions from limma R package v3.54.0[16]. Differentially expressed genes (DEGs) were identified based on a false discovery rate (FDR) < 0.05 and an absolute $\log_2$ fold change ($|\log_2(FC)|$) > 0.3. Over-representation analysis (ORA) was performed by querying the DEGs list against GO Biological Process 2025 gene-set library by enrichR R package v3.1[17]. Bubble plots of the top ten pathway terms for each condition (FDR < 0.05) were generated using ComplexHeatmap R package v2.14.0[18]. Clustering was performed with the ward.D method and Pearson's correlation distance to generate a heatmap using pheatmap function from ComplexHeatmap R package v2.14.0 and scaling the rows. Principal component analysis (PCA) was performed using FactoMineR R package v2.7[19] (Lê et al. 2008) and visualization of PCA results was achieved through Factoextra R package v1.0.7[20].

Results

Gene Ontology Functional Enrichment Analysis of Differentially Expressed Genes

Gene Ontology (GO) enrichment analysis was performed separately for upregulated and downregulated genes in MIO-M1 human Müller cells following stimulation with subthreshold 520 nm laser at 100 mW and 200 mW, compared with untreated controls. Functional enrichment was analyzed across the three principal GO domains: Biological Process (BP), Molecular Function (MF), and Cellular Component (CC). Only significantly enriched terms (FDR-adjusted $p < 0.05$) were considered.

Upregulated Genes – 100 mW Group

In the 100 mW-treated group, enrichment analysis revealed a predominant activation of pathways associated with cellular stress response, inflammatory modulation, and redox homeostasis.

Biological Process

The most significantly enriched BP categories included:

- *Response to oxidative stress*
- *Regulation of inflammatory response*
- *Cellular response to cytokine stimulus*
- *Regulation of NF-κB signaling*
- *Apoptotic process modulation*

Molecular Function

Enriched molecular function terms included:

- *Antioxidant activity*
- *Cytokine receptor binding*
- *Transcription factor binding*
- *Ion channel regulator activity*

These results support the hypothesis that laser stimulation promotes functional modulation of signaling pathways involved in oxidative balance and cellular communication rather than structural remodeling at this power level.

Cellular Component

Cellular Component enrichment analysis demonstrated overrepresentation of:

- *Plasma membrane components*
- *Cell junction complexes*
- *Cytoplasmic vesicles*

Although junction-related components were present, their enrichment was less pronounced compared with the 200 mW group.

Upregulated Genes – 200 mW Group

The 200 mW-treated group demonstrated a broader and more structurally oriented transcriptional activation pattern, with significant enrichment of pathways related to barrier integrity, ion transport, extracellular matrix organization, and endothelial interaction.

Biological Process

The most significantly enriched biological process categories included:

- *Cell–cell junction organization*
- *Tight junction assembly*
- *Regulation of endothelial cell permeability*
- *Extracellular matrix organization*
- *Ion transport and potassium ion transmembrane transport*
- *Water homeostasis*

Molecular Function

Significant molecular function enrichment included:

- *Structural molecule activity*
- *Cell adhesion molecule binding*
- *Ion channel activity*
- *Transmembrane transporter activity*

Cellular Component

Cellular component terms significantly enriched in the 200 mW group comprised:

- *Adherents junction*
- *Tight junction*
- *Basolateral plasma membrane*
- *Extracellular matrix*

Downregulated Genes

Downregulated genes in both 100 mW and 200 mW groups showed enrichment in processes related to:

- *Pro-inflammatory signaling pathways*
- *Positive regulation of cytokine production*
- *Angiogenic signaling cascades*
- *Cell proliferation pathways*

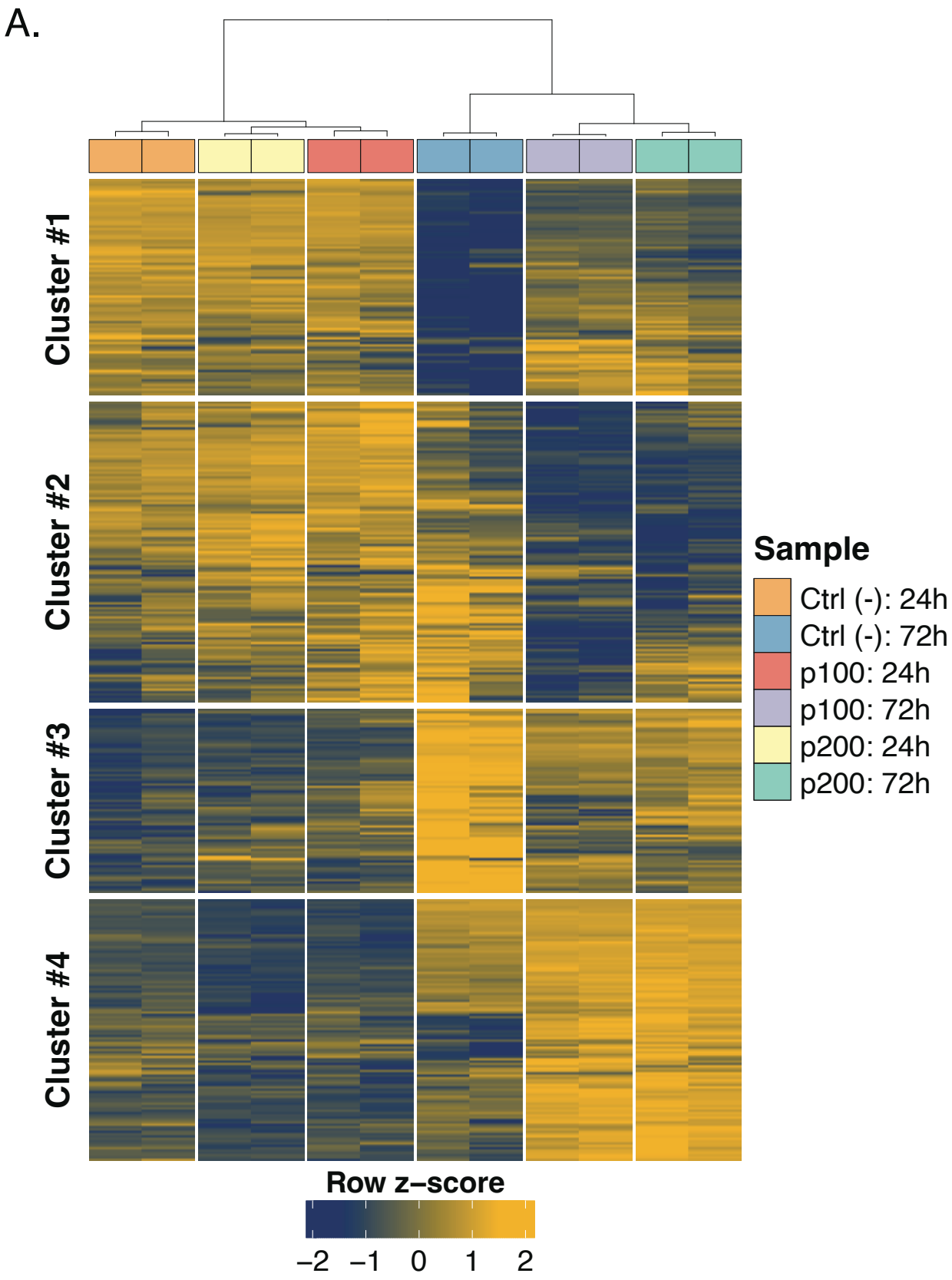

Figure 3 – Heat map of aggregate gene expression analysis

B.

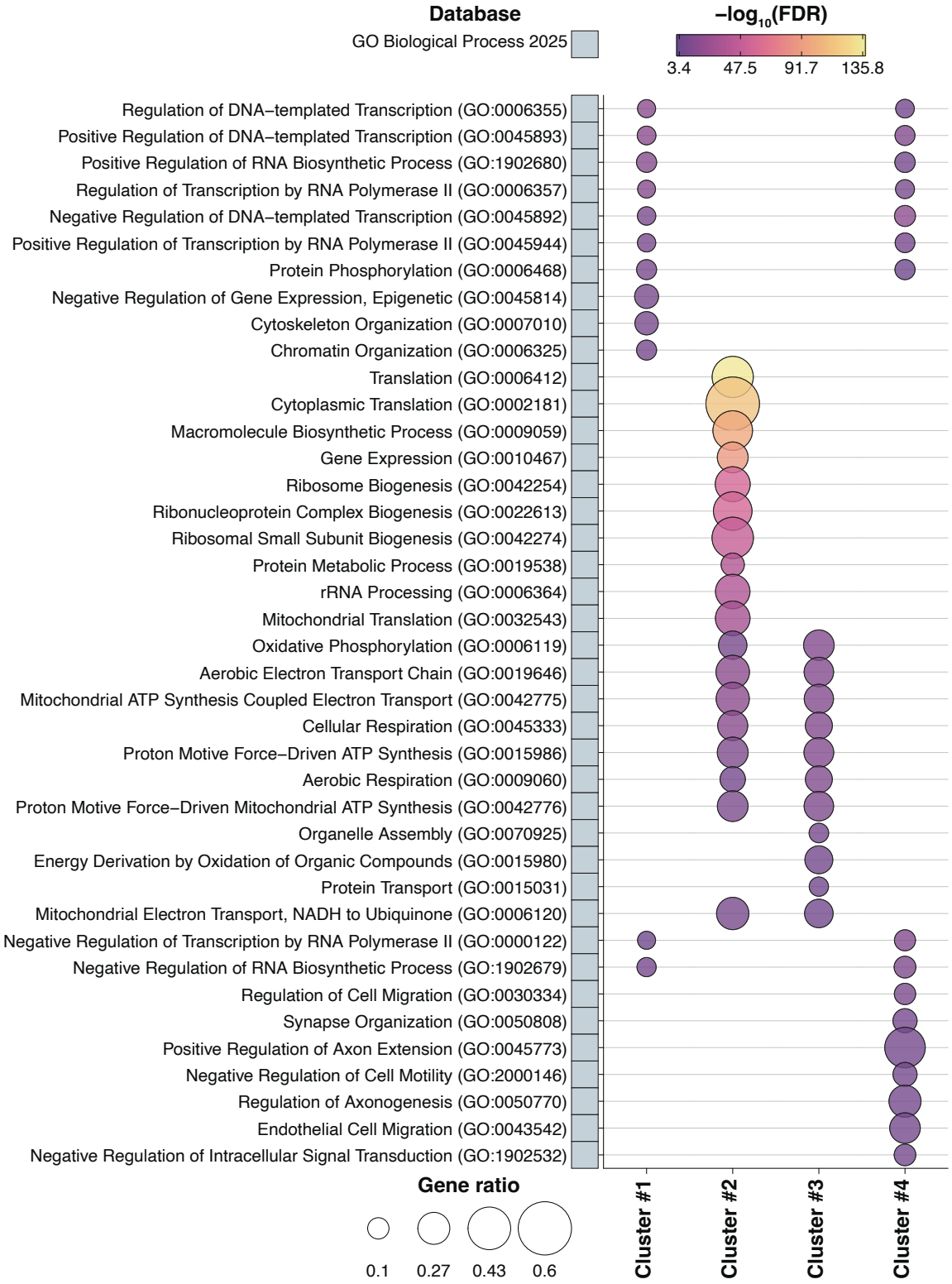

Figure 4 – Gene Ontology cluster analysis

Differential Gene Expression in MIO-M1 Cells After 200 mW Subthreshold Laser Stimulation

Differential gene expression analysis of laser-stimulated MIO-M1 Müller cells identified a subset of genes significantly up-regulated and down-regulated that are functionally associated with ion transport, osmotic regulation, vascular signaling, extracellular matrix organization, oxidative stress pathways, and glial-associated signaling mechanisms.

200 mW - Upregulated Genes

Ion Channels and Transporters

Gene	Log(FC)	FDR
KCNE2	1,49496791	0,00721193
KCNK3	1,15510931	0,04299647
KCNH2	1,13096417	0,00322117
KCND1	1,11152239	0,00288799
SLC45A1	0,99896938	0,02599055
SLC12A7	0,80984404	0,00318388
SLC38A3	0,69009321	0,00046229
SLC6A9	0,54943370	0,00234624
KCNK6	0,53835219	0,04519639
SLC12A4	0,50465927	0,00111709
SLC1A4	0,48753489	0,00166089
SLC27A1	0,45616699	0,00253953
KCNN4	0,44729517	0,01116032
SLC16A3	0,44668961	0,00151584
SLC27A4	0,42263816	0,01048579
SLC1A5	0,41993720	0,00624117
SLC22A5	0,37391345	0,01034061
SLC2A1	0,35937755	0,00496867

Gene	Log(FC)	FDR
SLC4A2	0,34341522	0,00251234
SLC2A3	0,30708657	0,01875759
KCNJ2	0,59336684	0,04357802
KCNAB2	0,38578540	0,03028455

Vascular and Growth Factor Signaling

Gene	Log(FC)	FDR
ENG	0,54982094	0,01539163
EPHB4	0,52651966	0,00114031
VEGFA	0,50152263	0,00276498
PDGFRB	0,45541916	0,00051162
PDGFA	0,45047558	0,00222275
VEGFB	0,44159531	0,01034061
EPHB2	0,41706208	0,00949701

Extracellular Matrix and Adhesion

Gene	Log(FC)	FDR
ITGB4	0,97886694	0,00013723
COL1A1	0,78835067	0,00020714
ITGB2	0,68411646	0,02942741
ITGA9	0,61493120	0,01491907
FN1	0,44390975	0,00063021
COL6A1	0,43846761	0,00088550
COL6A2	0,40921983	0,00402518
ITGA5	0,41357407	0,00160723
VCAM1	0,37647050	0,04055502
COL1A2	0,37526837	0,00193301

Gene	Log(FC)	FDR
VCAN	0,37091026	0,00584286
COL4A2	0,33050683	0,00548085
TNC	0,30015986	0,00579088

Glial and Inflammatory Signaling

Gene	Log(FC)	FDR
SOCS1	1,31516791	0,00341014
IRF7	0,73990901	0,02825140
GFAP	0,56692925	0,03635806
RELB	0,44616545	0,03780636
IRF1	0,44056871	0,00465136
TNFAIP3	0,36951352	0,03050644
NFKBIA	0,36294770	0,02893850
STAT3	0,30823414	0,00163178

200 mW – Downregulated Genes

Ion Transporters and Channels

Gene	Log(FC)	FDR
SLC25A27	-1,4752491	0,00310754
SLC38A4	-1,1841487	0,00674833
MCOLN3	-0,6204267	0,01963237
SLC7A11	-0,5971091	0,0003533
SLC16A9	-0,5264385	0,00385908
SLC25A14	-0,4639912	0,01399423
SLC25A20	-0,4326363	0,01268292
SLC25A12	-0,4231398	0,01590924
SLC25A36	-0,4161751	0,00188987

Gene	Log(FC)	FDR
SLC36A4	-0,3464381	0,04169828
SLC30A9	-0,3360844	0,00894897
KCMF1	-0,3352089	0,00178352
TRPM7	-0,3347395	0,00144665

Extracellular Matrix

Gene	Log(FC)	FDR
ECM2	-0,9229416	0,0120167
MMP16	-0,4910739	0,00071311
CLDN12	-0,3740364	0,00973067
FAP	-0,3735561	0,01106293

Redox-Related Genes

Gene	Log(FC)	FDR
TXNRD1	-0,5453653	0,00134812
NQO1	-0,4793605	0,00554839
PRDX1	-0,3753146	0,00913204
TXN	-0,3650604	0,0493978
PRDX3	-0,3098754	0,01502536

Signaling Molecules

Gene	Log(FC)	FDR
SGK1	-0,4425585	0,00267518
NRAS	-0,3523686	0,005152
MAPK8	-0,3365991	0,01760952

Differential Gene Expression in MIO-M1 Cells After 100 mW Subthreshold Laser Stimulation

Differential expression analysis following 100 mW laser stimulation identified a distinct transcriptional profile characterized by significant up-regulation and down-regulation of genes involved in ion transport, extracellular matrix organization, vascular signaling, ribosomal machinery, and non-coding RNA processing.

100 mW – Upregulated Genes

Ion Channels and Transporters

Gene	Log(FC)	FDR
SCNN1A	2,863547327	0,004119634
SLC29A2	1,553292924	0,02817313
SLC37A1	1,358073592	0,032316659
SLC45A1	1,030606137	0,021409936
SLC47A1	0,931688352	0,025285008
KCNB1	0,705526369	0,020442983
SLC45A4	0,662177061	0,007995893
KCNH2	0,588409918	0,038089235
SLC1A1	0,584822848	0,031946931
SLC12A7	0,576287257	0,011170753
KCNJ2	0,57332523	0,040009221
KCNC4	0,537002842	0,00136135
SLC1A4	0,530876946	0,000727385
SLC2A3	0,522582041	0,001063929
SLC27A1	0,519365213	0,000955235
SLC6A9	0,479654124	0,003217078

Vascular and Growth Factor Signaling

Gene	Log (FC)	FDR
VEGFA	0,417388174	0,00524717
NRP1	0,409916364	0,001432371
PDGFA	0,377115045	0,003940493
TGFB1	0,350941005	0,013147617
PDGFRB	0,347374388	0,001371157
VEGFB	0,329665328	0,031955209

Extracellular Matrix and Adhesion

Gene	Log (FC)	FDR
COL1A1	0,819179535	9,26E-05
ITGB4	0,711940111	0,000338856
COL5A1	0,551728377	0,000164947
ITGA5	0,478724965	0,000569496
FN1	0,397686649	0,000810735
COL1A2	0,395797677	0,00109562
COL6A1	0,337852422	0,002381806
COL4A2	0,330775452	0,004364969
COL6A2	0,326675274	0,010090041
VCAN	0,323204322	0,000550861
TNC	0,309505251	0,004068514

100 mW – Downregulated Genes

Ion Transporters and Channels

Gene	Log (FC)	FDR
ASIC3	-0,974775	0,01188652
MCOLN3	-0,7922608	0,00426555
SLC16A9	-0,6710205	0,00075961

Gene	Log (FC)	FDR
SLC25A20	-0,4995	0,0053925
SLC7A11	-0,4139764	0,00144573
SLC30A9	-0,353303	0,00585071
SLC25A36	-0,3138564	0,00558588

Redox-Related Genes

Gene	Log (FC)	FDR
NQO1	-0,6933353	0,00068955
TXN	-0,5553638	0,00671746
PRDX1	-0,4804878	0,00219188
TXNRD1	-0,4669035	0,00203014
PRDX3	-0,4683649	0,00152389

Extracellular Matrix

Gene	Log (FC)	FDR
ECM2	-0,9983243	0,00755818
COL4A3	-0,6436939	0,00147343
FAP	-0,5089045	0,00174826

Signaling Molecules

Gene	Log (FC)	FDR
RGS4	-0,5006584	0,00075961
SGK1	-0,4518145	0,00167527
MAPK8	-0,3833174	0,00767892
TLR4	-0,3523239	0,02791862

Mitochondrial Genes

Gene	Log (FC)	FDR
MT-ND3	-2,893693	0,01028482
MT-ND2	-2,6891215	0,02223191
MT-CO2	-2,6625408	0,01127113
MT-ATP6	-2,6172652	0,01986199
MT-ND5	-2,4391129	0,01507904
MT-ND4	-2,3835762	0,01447876
MT-ND1	-1,7592729	0,01824296
MT-ND6	-1,7177397	0,01626308
MT-CO3	-0,6960754	0,0353475

Discussion

Transcriptomic Safety Profile of Subthreshold Laser Stimulation

An important aspect of the present transcriptomic analysis concerns the safety profile of subthreshold 520 nm laser stimulation at the molecular level. The differential gene expression patterns observed in both the 100 mW and 200 mW groups did not reveal activation of canonical apoptotic or cell death pathways. Specifically, no coordinated upregulation of key mediators of intrinsic or extrinsic apoptosis—such as CASP3, CASP7, CASP8, CASP9, BAX, BAK1, FAS, FADD, or TNFRSF family members—was detected. Furthermore, no enrichment of Gene Ontology categories related to “apoptotic process,” “programmed cell death,” “intrinsic apoptotic signaling pathway,” or “necrotic process” emerged from the analyzed datasets [21]. This absence of a pro-apoptotic transcriptional signature suggests that the applied laser parameters did not induce overt cytotoxic stress at the cellular level.

Although isolated stress-related genes were modulated, their expression changes were not organized into a coherent cell death program. For instance, genes classically involved in mitochondrial-mediated apoptosis or p53-dependent death pathways were not collectively upregulated. Similarly, no transcriptional evidence of ferroptosis (e.g., coordinated modulation of GPX4, ACSL4, lipid peroxidation-related enzymes), necroptosis (RIPK1/RIPK3/MLKL axis), or inflammasome-driven pyroptosis was observed. Even in the 100 mW group, where a marked downregulation of several mitochondrial-encoded genes was detected, this pattern was not accompanied by activation of pro-apoptotic mediators, suggesting metabolic reprogramming rather than mitochondrial collapse or cell death induction.

These findings are consistent with the established biological rationale of subthreshold micropulse laser therapy, which is designed to induce a bio-modulatory response without causing thermal coagulation or structural retinal damage[22–24]. Clinical and imaging studies have demonstrated the absence of

visible retinal scarring or photoreceptor disruption following properly delivered subthreshold treatment, supporting its non-destructive nature. The present transcriptomic data extend and reinforce this concept to molecular level, indicating that laser-induced response reflects adaptive cellular regulation rather than injury-driven degeneration.

Taken together, the absence of a transcriptional cell death signature reinforces the safety profile of subthreshold laser stimulation under the tested conditions. While transcriptomic data cannot fully exclude subtle or delayed cellular effects, the lack of coordinated activation of apoptotic or necrotic pathways strongly supports the interpretation that the observed gene expression changes represent regulated biological adaptation rather than laser-induced cytotoxicity.

Muller cell activation

The observed upregulation of the GFAP gene following subthreshold laser stimulation provides molecular evidence of Müller cell activation. Glial fibrillary acidic protein (GFAP) is a well-established marker of reactive gliosis in the retina and is specific of Müller cells under physiological conditions, becoming transcriptionally upregulated in response to stress, injury, or microenvironmental perturbation[25]. The moderate increase in GFAP expression detected in our dataset, however, was not accompanied by a broad transcriptional signature of inflammation, apoptosis, or extracellular matrix scarring. This pattern may suggest that the laser-induced GFAP upregulation likely reflects a controlled and adaptive glial activation rather than a full gliotic response. In the context of subthreshold laser therapy, which is designed to induce bio-modulatory rather than destructive effects, a limited increase in GFAP expression may represent a physiological activation state of Müller cells aimed at restoring tissue homeostasis and supporting retinal fluid regulation. Therefore, the magnitude and molecular context of GFAP upregulation in this study are more consistent with a regulated activation process than with pathological gliosis.

Fluid Homeostasis and Müller Cell–Mediated Ionic Regulation

The transcriptional profile observed following subthreshold 520 nm laser stimulation suggests activation of gene networks potentially involved in retinal fluid homeostasis. Retinal water balance is primarily regulated by the coordinated interaction between the retinal pigment epithelium (RPE) and Müller glial cells. While the RPE drives transepithelial fluid transport toward the choroid, Müller cells regulate extracellular ionic composition, spatial potassium redistribution, and osmotic gradients within the neural retina [26,27].

In classical models of retinal edema regulation, Müller cells control extracellular K^+ concentration through inwardly rectifying potassium channels (Kir4.1, encoded by KCNJ10) functionally coupled to aquaporin-4 (AQP4), thereby enabling coordinated potassium siphoning and water transport[28]. Notably, neither KCNJ10 nor AQP4 emerged among the differentially expressed genes in the present study. This absence suggests that our subthreshold laser stimulation does not act via transcriptional upregulation of canonical Müller water channels.

Instead, the data indicate modulation of a broader spectrum of solute carriers and potassium channel subunits.
Several SLC transporters (e.g.SLC1A1, SLC1A4, SLC12A7, SLC27A1, SLC6A9) and voltage-gated potassium channels (e.g.KCNB1, KCNH2, KCNJ2, KCNC4) were upregulated. These molecules participate in amino acid transport, chloride-coupled ion movement, and potassium conductance, all of which influence osmotic balance[29]. Even in the absence of direct aquaporin transcriptional modulation, changes in ion transporter expression can modify osmotic gradients, thereby indirectly affecting water movement across Müller membranes. Such a mechanism would be consistent with a regulatory rather than structural response to stimulation.

Furthermore, downregulation of selected transporters (e.g., SLC16A9, SLC7A11) and mitochondrial carriers may reflect metabolic adjustments in glial cells. Müller cells are metabolically dynamic and respond to stress or stimulation by

altering glycolytic and mitochondrial pathways, which can secondarily influence ion transport capacity. A transient metabolic recalibration, rather than overt dysfunction, could contribute to restoration of extracellular ionic stability and reduction of intraretinal fluid accumulation.

Importantly, subthreshold micropulse laser has been described as a non-damaging therapy that induces a biological response rather than thermal coagulation[10,24,30]. The present findings are compatible with this concept: instead of evidence of necrotic signaling or barrier breakdown, the dataset suggests activation of intrinsic regulatory mechanisms. While direct functional confirmation is lacking, the coordinated modulation of ion transporters and channels supports the hypothesis that subthreshold laser stimulation may enhance Müller cell–mediated ionic buffering and thereby contribute to macular fluid stabilization.

Modulation of the Extracellular Matrix and Tissue Microenvironment

Beyond ionic transport, the transcriptional response indicates significant modulation of extracellular matrix (ECM) components and adhesion molecules. Upregulation of structural ECM genes—including COL1A1, COL1A2, COL4A2, COL5A1, COL6A1, COL6A2, FN1, VCAN, TNC, ITGA5, and ITGB4—suggests active remodeling of the retinal microenvironment.

Müller cells are not only ionic regulators but also structural scaffolds spanning the entire retinal thickness. They synthesize and organize extracellular matrix components and contribute to the integrity of the inner limiting membrane and perivascular support structures[27]. Controlled ECM remodeling may influence retinal compliance, interstitial diffusion properties, and vascular–glial interactions. In the context of macular edema, ECM composition affects both barrier permeability and mechanical resistance to fluid accumulation.

The upregulation of integrins (ITGA5, ITGB4) and matrix proteins such as fibronectin and collagen could reflect reinforcement or reorganization of cell–matrix interactions rather than fibrotic activation. Importantly, subthreshold

laser treatment has been associated clinically with gradual anatomical improvement without inducing scarring or visible coagulative damage[10,24]. Therefore, ECM gene activation in this setting may represent adaptive tissue stabilization rather than pathological fibrosis.

Conversely, downregulation of selected matrix-associated genes (e.g., ECM2, FAP, COL4A3) in the 100 mW dataset suggests selective remodeling rather than uniform matrix expansion. Such bidirectional modulation indicates a dynamic rebalancing process. From a mechanistic perspective, stabilization of the extracellular matrix may reduce abnormal interstitial fluid diffusion and support restoration of barrier function. However, given the absence of protein-level validation, these interpretations remain cautious and hypothesis-generating.

Redox Pathway Modulation and Oxidative Stress Regulation

Oxidative stress plays a well-established role in the pathophysiology of diabetic macular edema and other forms of retinal edema, contributing to endothelial dysfunction, inflammation, and barrier breakdown. In the present study, both 100 mW and 200 mW stimulation were associated with modulation of redox-related genes, including NQO1, PRDX1, PRDX3, TXN, and TXNRD1.

Interestingly, several of these genes were downregulated following stimulation. While at first glance this might suggest reduced antioxidant capacity, it may alternatively indicate a decrease in oxidative stress signaling demand. In a state of active oxidative injury, antioxidant genes are typically upregulated as a compensatory response. Therefore, their relative downregulation after laser stimulation could reflect normalization of redox homeostasis rather than suppression of protective mechanisms[31].

Subthreshold laser has been proposed to induce a mild, controlled cellular stress that triggers adaptive responses without causing structural damage[23,24]. Such a response could recalibrate redox-sensitive transcription pathways,

including NF-κB and MAPK-related signaling cascades, which were also modestly modulated in the dataset. Müller cells are highly sensitive to oxidative stress and play a central role in redox buffering within the retina. Thus, modulation of thioredoxin and peroxiredoxin systems may reflect glial adaptation toward a more balanced oxidative state.

Moreover, immortalized cell lines may exhibit a constitutively elevated expression of redox-regulating genes such as *NQO1, PRDX1, PRDX3, TXN,* and *TXNRD1*. This phenomenon is biologically plausible, as immortalization is typically associated with increased proliferative activity, metabolic reprogramming, and altered mitochondrial function, all of which can lead to enhanced basal production of reactive oxygen species (ROS). To maintain redox homeostasis and sustain cell survival, these cells often upregulate antioxidant defense systems, including the NRF2 pathway and the thioredoxin–peroxiredoxin axis. Consequently, the baseline redox profile of immortalized cells may not fully reflect physiological conditions, and apparent downregulation of antioxidant genes following experimental treatment may represent normalization from an intrinsically elevated oxidative state rather than impairment of cellular defense mechanisms[32].

Taken together, the redox-related transcriptional changes are consistent with a shift toward a stabilized metabolic and inflammatory microenvironment. Given that oxidative stress is a known driver of vascular permeability and fluid leakage, reduction or normalization of redox signaling may indirectly support fluid resorption and barrier recovery.

Conclusions

The present transcriptomic analysis provides novel insights into the molecular effects of subthreshold 520 nm laser stimulation on human Müller cell–derived MIO-M1 cultures. Under the experimental conditions adopted, both 100 mW and 200 mW laser exposure induced measurable but non-destructive transcriptional modulation across pathways involved in ion transport, extracellular matrix organization, vascular signaling, metabolic regulation, and redox balance.

Importantly, the gene expression profile did not reveal coordinated activation of canonical apoptotic or cell death pathways. The absence of transcriptional upregulation of key mediators of intrinsic and extrinsic apoptosis, together with the lack of enrichment of Gene Ontology categories related to programmed cell death, supports the interpretation that subthreshold laser stimulation at the tested parameters does not induce overt cytotoxicity. This finding is consistent with the established bio-modulatory nature of subthreshold laser therapy and reinforces its favorable molecular safety profile.

From a mechanistic perspective, the most consistent transcriptional signal across the datasets concerned modulation of genes implicated in ionic transport and solute handling, alongside remodeling of extracellular matrix components and regulation of oxidative stress–related pathways. Although canonical water-channel genes such as AQP4 and KCNJ10 (Kir4.1) were not differentially expressed, the broader modulation of potassium channels and solute carrier family members suggests a potential reorganization of ionic flux regulation. Given the central role of Müller cells in retinal potassium buffering and osmotic equilibrium, these changes are compatible with activation of intrinsic homeostatic mechanisms that may indirectly influence retinal fluid balance.

Furthermore, the modulation of extracellular matrix and adhesion-related genes indicates that subthreshold laser stimulation may influence the structural microenvironment in which Müller cells operate. Controlled remodeling of matrix components could affect tissue compliance, barrier properties, and

intercellular signaling. Similarly, the observed changes in redox-related genes suggest a recalibration of oxidative stress pathways rather than activation of injurious stress responses. Taken together, these findings support a model in which subthreshold laser stimulation induces adaptive, regulatory cellular responses rather than degenerative processes.

Limitations

The conclusions of the present study must be interpreted within the context of several limitations. First, the experiments were conducted in a Müller cell line under basal, non-pathological conditions. Retinal edema in clinical settings typically arises in a background of hypoxia, inflammation, metabolic dysregulation, and vascular leakage. Therefore, the transcriptional effects observed in healthy cultured cells may not fully recapitulate the biological responses occurring in diseased retinal tissue. Second, transcriptomic changes do not necessarily translate into functional protein-level alterations, nor do they directly demonstrate improved fluid transport capacity.

Future perspectives

Future investigations are therefore warranted to clarify the functional implications of these findings. In vitro studies employing Müller cells exposed to hypoxic stress, inflammatory cytokines, or high-glucose conditions would allow evaluation of whether subthreshold laser stimulation can reverse or attenuate gene expression signatures associated with retinal edema pathophysiology. Such models would be particularly informative for assessing modulation of hypoxia-inducible pathways, oxidative stress responses, and barrier-related signaling in a context that more closely mimics clinical disease. In parallel, in vivo studies in established models of retinal edema—such as ischemia-induced, diabetic, or vascular occlusion models—are necessary to determine whether the transcriptional adaptations observed here translate into measurable anatomical and functional improvements. Integration of transcriptomic data with protein quantification, electrophysiological

assessments, and imaging-based evaluation of retinal thickness would provide a more comprehensive understanding of the mechanism of action.

Final considerantions

In conclusion, the present analysis suggests that subthreshold 520 nm laser stimulation induces regulated, non-cytotoxic transcriptional adaptations in Müller cells, involving pathways potentially relevant to retinal fluid homeostasis, extracellular matrix remodeling, and redox balance. While these findings are mechanistically suggestive, definitive conclusions regarding therapeutic action require further validation in disease-relevant experimental systems. Carefully designed in vitro and in vivo studies under hypoxic and metabolically stressed conditions will be essential to elucidate the precise biological mechanisms underlying the clinical efficacy of subthreshold laser therapy in macular edema.

Chapter 2
OCT Retinal biomarkers
The role of Müller cell cone in macular edema secondary to retinal vein occlusion

Introduction

Retinal vein occlusion (RVO) is one of the most prevalent retinal vascular disorders and represents a major cause of vision loss worldwide, ranking second only to diabetic retinopathy among retinal vascular diseases. In 2015, the global prevalence of any RVO, in people aged 30-89 years was 0.77%, equivalent to an overall of 28.06 million worldwide. Hypertension is the strongest risk factor for any RVO, with a meta- odds ratio (OR) of 2.82[33].

Clinically, RVO is classified into central retinal vein occlusion (CRVO) and branch retinal vein occlusion (BRVO), entities that differ in terms of vascular involvement, ischemic areas, and visual prognosis. Despite these differences, macular edema is the most frequent and visually significant complication across the RVO disease spectrum and remains the primary target of therapeutic intervention. Consequently, identifying reliable structural and functional biomarkers that reflect disease severity, potentially predict visual outcomes, and guide treatment decisions is important[34–45].

OCT biomarkers

Optical coherence tomography (OCT) has become an indispensable imaging modality in the management of RVO-associated macular edema, owing to its ability to provide non-invasive, high-resolution visualization of retinal microstructure. Over the past decade, OCT has enabled the identification of a wide range of quantitative and qualitative biomarkers, including central retinal thickness (CRT), disorganization of retinal inner layers (DRIL), integrity of the external limiting membrane (ELM) and ellipsoid zone (EZ), hyperreflective foci (HRF), intraretinal cystoid spaces, subretinal fluid (SRF), and more recently described features such as foveal eversion [34–45]. These biomarkers have been widely investigated for their associations with baseline visual acuity, functional recovery, and response to intravitreal therapies.

Traditionally, the pathogenesis of macular edema in RVO has been attributed primarily to increased vascular permeability resulting from venous outflow obstruction, capillary non-perfusion, and upregulation of vascular endothelial growth factor (VEGF). This vascular-centric model has provided the rationale for the widespread use of anti-VEGF agents as first-line therapy, with long lasting intravitreal corticosteroids targeting the inflammatory component of the disease and used as a second line treatment or in a co-treatment scheme. However, clinical experience and emerging evidence indicate that vascular leakage alone does not fully explain the heterogeneity observed in treatment response and long-term visual outcomes. Indeed, a substantial proportion of eyes demonstrate persistent or recurrent macular edema despite adequate suppression of VEGF, while others exhibit limited functional recovery despite anatomical improvement[34–40].

In recent years, increasing attention has been directed toward the role of retinal neuroglial elements, particularly the Müller cell complex, in the development and persistence of macular edema. Müller cells span the entire thickness of the retina and play a central role in maintaining retinal homeostasis, including regulation of extracellular fluid, potassium buffering, metabolic support of neurons, and preservation of retinal architecture. Dysfunction of Müller cells has been implicated in impaired fluid clearance, disruption of synaptic transmission, and loss of structural integrity within the inner retina. OCT has provided indirect but clinically relevant markers of this dysfunction, linking imaging findings to underlying cellular pathology [35,46].

Among OCT biomarkers, DRIL has emerged as one of the most consistently reported predictors of poor visual function in RVO-associated macular edema. DRIL is defined as the loss of identifiable boundaries between the ganglion cell–inner plexiform layer complex, inner nuclear layer, and outer plexiform layer over a given retinal segment. Multiple studies have demonstrated that the presence and extent of DRIL are strongly associated with worse baseline visual acuity and poorer visual outcomes following treatment[34,35,37–42]. Importantly, DRIL is increasingly regarded not merely as a structural abnormality but as a surrogate marker of Müller cell impairment, supported by imaging and molecular evidence linking DRIL to markers of glial stress and dysfunction [45,47].

The integrity of the outer retinal layers, particularly the ELM and EZ, represents another key OCT-derived biomarker in RVO. Disruption of these layers has been repeatedly associated with reduced visual acuity at baseline and worse short-term visual outcomes following anti-VEGF or steroid therapy [34,35,37,38]. However, longitudinal studies and systematic reviews suggest that while ELM and EZ integrity may predict early functional recovery, but their prognostic value tends to diminish over longer follow-up periods or after repeated treatments, indicating that outer retinal restoration alone may be insufficient to ensure sustained visual improvement [44,48].

Hyperreflective foci are frequently observed in eyes with RVO-related macular edema and are generally interpreted as markers of inflammatory activity, lipid extravasation, or activated microglial cells. Several studies have reported associations between higher HRF counts and worse visual acuity or increased disease severity [34,35,40]. Nevertheless, the clinical utility of HRF as a prognostic biomarker remains limited by the lack of standardized definitions, variability in quantification methods, and inconsistent reporting of their retinal localization across studies [44,48].

More recently, novel OCT features linked to Müller cell dysfunction have been described. Foveal eversion, characterized by an outward displacement of the inner retinal layers at the fovea, has been identified as a marker of advanced disease and is associated with persistent or refractory macular edema and progressive visual deterioration [45]. Similarly, microcystic macular edema localized to the inner nuclear layer has been proposed as a manifestation of neuroglial dysfunction rather than simple vascular leakage, further supporting the concept that glial pathology plays a critical role in disease chronicity [49].

Studies combining OCT findings with proteomic and cytokine analyses have demonstrated correlations between intraretinal or SRF compartments and activation of inflammatory, immune, oxidative stress, and complement pathways, implicating Müller cells as active participants in these processes [36,50]. In addition, en face OCT techniques have enabled the visualization and

quantification of macrophage-like cells at the vitreoretinal interface, whose density has been shown to correlate with macular thickness and edema severity [51,52].

OCT-based structural biomarkers constitute essential tools for the evaluation of macular edema secondary to retinal vein occlusion and are promising in determine the functional recovery. Biomarkers reflecting Müller cell complex integrity—particularly DRIL and foveal architecture abnormalities—appear to play a central role in linking retinal microstructural changes to functional outcomes.

The Müller cell cone as an anatomical and imaging concept

The Müller cell cone represents a specialized glial structure located in the central fovea. It was described by Gass as a cone-shaped zone of Müller cells forming the central and inner portion of the fovea centralis, with a hypothesized role in maintaining foveal structural integrity and in the pathogenesis of selected macular disorders, including macular hole and foveal retinoschisis[53]. This concept remains less familiar than other OCT biomarkers, but it is highly relevant when considering the neuroglial contribution to foveal architecture.

Anatomically, the Müller cell cone is composed of specialized Müller cells located in the foveola, extending from the outer limiting membrane toward the inner limiting membrane. Unlike the elongated Müller cells of the foveal walls, these central foveolar Müller cells form an inverted cone-like configuration that contributes to the mechanical stabilization of the foveal center. Because Müller cells are involved in retinal fluid regulation, ionic homeostasis, metabolic support, and structural organization, disruption of the Müller cell cone may reflect a loss of foveal neuroglial integrity rather than a simple consequence of retinal thickening.

In OCT-based assessment, preservation of the Müller cell cone hag gained research attention and can be interpreted as an indirect marker of maintained foveal architecture, whereas its disruption, flattening, or outward displacement may indicate advanced structural disorganization of the foveal center. For this reason, evaluation of the Müller cell cone may provide complementary information to established biomarkers such as central retinal thickness, DRIL, ELM integrity, and EZ/IZ continuity.

Aim of the Study

The aim of this study is to evaluate structural alterations of the Müller cell cone (MCC) in eyes with macular edema secondary to retinal vein occlusion, as assessed by optical coherence tomography (OCT), and to determine their association with anatomical persistence of macular edema after a standard loading phase of three intravitreal anti-VEGF injections.

In particular:

1. To investigate the relationship between Müller cell cone alteration and outer retinal integrity, as assessed by OCT evaluation of the external limiting membrane (ELM) and interdigitation zone/ellipsoid zone (IZ/EZ) continuity at baseline and after three anti-VEGF injections.
2. To evaluate the potential role of Müller cell cone alterations as a biomarker of disease severity, by analyzing its association with CRT and Visual acuity.

Material and Methods

Study Design and Population

This study was designed as a retrospective observational cohort study. Patients were consecutively recruited and followed at the **SC Oculistica, Ospedale di Circolo e Fondazione Macchi, Varese, Italy**, over a time interval extending from July 2020 to April 2024.
Eligible subjects were adult patients (≥18 years) diagnosed with retinal vein occlusion (RVO), either branch retinal vein occlusion (BRVO) or central retinal vein occlusion (CRVO), complicated by macular edema (ME). The diagnosis was established through multimodal imaging, including structural spectral-domain optical coherence tomography (SD-OCT).

Inclusion Criteria

Patients were included if they met all the following criteria:

1. Age ≥18 years.
2. Diagnosis of BRVO or CRVO complicated by center-involving macular edema.
3. Treatment-naïve status at baseline (no prior intravitreal therapy).
4. Management with a single loading cycle of three consecutive monthly intravitreal anti-VEGF injections.
5. Use of either:
    - Ranibizumab (Lucentis®)
    - Aflibercept (Eylea®).

The anti-VEGF loading regimen was consistent with current therapeutic standards for RVO-associated macular edema and with protocols adopted in major randomized controlled trials and real-world studies.

Exclusion Criteria

To minimize confounding factors affecting visual acuity and retinal morphology, the following exclusion criteria were applied:

- Previous intravitreal treatments (anti-VEGF or corticosteroids).
- Prior vitreoretinal surgery.
- Previous intravitreal corticosteroid implants.
- History of focal/grid laser or panretinal photocoagulation for the study eye.
- Presence of significant media opacities impairing OCT image quality.
- High myopia (> −7.00 diopters).
- Amblyopia.
- Age-related macular degeneration (AMD).
- Diabetic macular edema or any macular edema secondary to causes other than RVO.
- Any other retinal maculopathy potentially influencing central visual acuity.
- Severe baseline structural disruption precluding reliable biomarker assessment.

Particular attention was paid to excluding macular edema secondary to diabetic retinopathy, given the well-documented role of Müller cell dysfunction and distinct inflammatory pathways in DME, which differ pathophysiologically from RVO-related macular edema

Final Study Sample

After application of all inclusion and exclusion criteria, a total of **82 eyes from 82 patients** were included in the final analysis. Each patient contributed only one eye to avoid inter-eye correlation bias. The cohort comprised both BRVO and CRVO cases, all treated with a standardized anti-VEGF loading regimen and followed longitudinally with structural SD-OCT imaging for biomarker evaluation.

OCT Image Acquisition and Analysis

Spectral-domain optical coherence tomography (SD-OCT) imaging was performed using standardized macular raster scan protocols centered on the fovea. Horizontal B-scan passing through the anatomical foveal center were selected for qualitative and quantitative analyses. All images were reviewed for adequate signal strength and quality prior to evaluation. OCT assessments were performed independently by masked graders with expertise in retinal imaging.

Assessment of Müller Cell Cone Structure

The Müller cell cone (MCC) structure was evaluated following the methodological approach described by Choi et al [54] (fig.1). Horizontal B-scans through the foveal center were analyzed to identify the characteristic hyperreflective, inverted cone-shaped structure located at the central fovea. An intact MCC was defined by the presence of a continuous, symmetrically shaped hyperreflective cone with preserved centripetal orientation of the inner retinal layers toward the foveal pit. MCC alteration was defined by disruption or loss of this hyperreflective structure, flattening or outward displacement of the inner retinal contour at the fovea, loss of the normal inverted cone configuration, or indistinct organization of the inner retinal layers at the foveal center. MCC status was classified dichotomously as intact or altered.

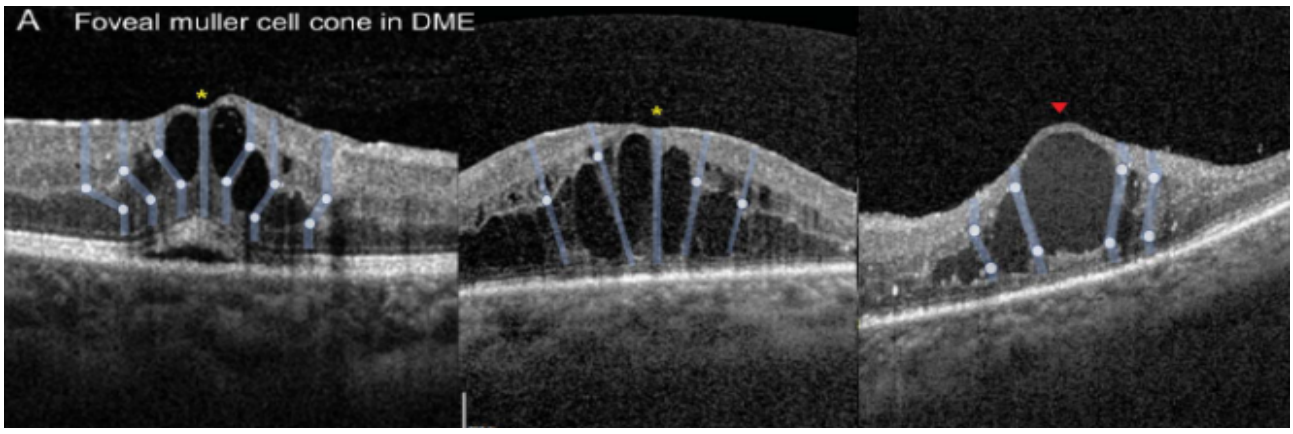

Figure 5- muller cell cone structure evaluation. In the first OCT on the left a preserved MCC morphology during macular edema; in the central OCT a partial disruption of the MCC with flattering and outward displacement; in the third OCT a complete disruption

Assessment of External Limiting Membrane and IZ/EZ Integrity

The integrity of the external limiting membrane (ELM) and interdigitation zone/ellipsoid zone (IZ/EZ) was evaluated on central horizontal and vertical OCT B-scans. Each layer was assessed separately.

An intact ELM was defined as a continuous, uninterrupted hyperreflective line across the central foveal region. ELM disruption was defined as focal or complete loss, discontinuity, or irregularity of this band at the foveal center.

Similarly, the IZ/EZ complex was evaluated based on the continuity and reflectivity of the hyperreflective band corresponding to photoreceptor inner segment ellipsoids and interdigitation with the retinal pigment epithelium. An intact IZ/EZ was defined as a continuous, well-demarcated band across the fovea, whereas IZ/EZ disruption was defined as any focal interruption, attenuation, or absence of the band at the foveal center.

For both ELM and IZ/EZ, integrity was classified dichotomously as intact or disrupted to allow correlation with MCC status and anatomical treatment response.

Retinal Thickness Measurements

Retinal thickness measurements were obtained from spectral-domain optical coherence tomography (SD-OCT) images using the device's automated segmentation software, with manual correction applied when necessary to ensure anatomical accuracy. Central retinal thickness (CRT) was defined as the mean retinal thickness within the central 1-mm diameter circle of the Early Treatment Diabetic Retinopathy Study (ETDRS) grid, measured from the internal limiting membrane to the retinal pigment epithelium. CRT values were recorded at baseline and after completion of the three-dose anti-VEGF loading phase.

All thickness measurements were reviewed for segmentation errors, particularly in the presence of cystoid changes or severe retinal distortion and corrected manually when required. CRT was analyzed as a continuous variable and used as an objective quantitative marker of macular edema severity.

Grading Procedure and Reproducibility

Both biomarker of MCC structure, and ELM and IZ/EZ integrity, were graded independently by masked observers. In cases of disagreement, images were evaluated by a third retinal specialist independently. This standardized qualitative grading approach was adopted to ensure reproducibility and consistency across biomarkers reflecting inner retinal organization, outer retinal integrity, and muller cell status.

Statistical Analysis

All statistical analyses were performed using R version 4.5.2 (The R Foundation).

Variable analyzed were:

- Visual Acuity (LogMAR)
- Central Retinal Thickness (CRT)
- ELM and IZ/EZ integrity

Continuous variables (logMAR and CRT) were initially explored for distributional characteristics using descriptive statistics and graphical inspection. Given the marked imbalance in sample size between groups (Müller cell cone integrity vs absence or alteration) and the absence of assumptions regarding normality and homoscedasticity, between-group comparisons were conducted using the Brunner–Munzel test, a non-parametric rank-based procedure that does not assume equal variances and is robust in the presence of heteroscedasticity.

The Brunner–Munzel test evaluates stochastic dominance between two independent groups and estimates the probability that a randomly selected observation from one group exceeds a randomly selected observation from the other group. For each comparison, the test statistic and corresponding two-sided p-value were reported. Statistical significance was set at $p < 0.05$.

In addition to hypothesis testing, the stochastic superiority effect size was calculated for each variable. This measure corresponds to:

$$P(X_{Müller+} > X_{Müller-}) + \frac{1}{2}P(X_{Müller+} = X_{Müller-})$$

and represents the probability that a randomly selected eye with Müller cell cone alteration shows a higher value than a randomly selected eye without alteration. Effect size magnitude was interpreted according to commonly accepted benchmarks for probabilistic indices (0.50 = no effect; 0.56–0.64 = small; 0.64–0.71 = moderate; >0.71 = large). All tests were two-tailed.

The association between Müller cell cone status (present vs absent) and outer retinal structural disruption (ELM/IS–OS integrity: disrupted vs preserved) was evaluated using an exact inferential approach for 2×2 contingency tables.

Given the small sample size of the Müller-negative subgroup and the presence of low expected cell counts, the classical asymptotic Pearson chi-square test was considered potentially unreliable. Therefore, the association was assessed using Barnard's exact test, an unconditional exact test for 2×2 tables.

Unlike Fisher's exact test, which conditions on fixed marginal totals, Barnard's test does not impose this constraint and is generally more powerful in small and unbalanced samples. A two-sided alternative hypothesis was used.

Effect size was expressed as the odds ratio (OR) derived from the contingency table. All statistical tests were two-sided, and statistical significance was defined a priori as $p < 0.05$.

Results

Descriptive Statistical Analysis

The analyzed cohort consisted of elderly patients (mean age approximately 74 years), with a balanced sex distribution and a predominance of BRVO over CRVO. These demographic and clinical characteristics are fully consistent with the epidemiological literature on retinal vein occlusions, in which advanced age represents the main systemic risk factor.

The variable are presented in the following table

Variable	**Value**
Age (years)	73.7 ± 11.3
Age range	30 – 90
Sex, n (%)	
Male	42 (51.2%)
Female	40 (48.8%)
RVO Type, n (%)	
BRVO (Branch Retinal Vein Occlusion)	49 (59.8%)
CRVO (Central Retinal Vein Occlusion)	33 (40.2%)

The study cohort was stratified according to the presence and integrity (Müller+) or absence or distruption (Müller−) of Müller cell cone and further subdivided based on the underlying retinal vein occlusion subtype.

A total of:

- 27 CRVO and 43 BRVO eyes were included in the Müller+ group
- 6 CRVO and 6 BRVO eyes were included in the Müller− group

Both functional (best-corrected visual acuity, BCVA, expressed in LogMAR) and anatomical (central retinal thickness, CRT, expressed in micrometers) parameters were analyzed at baseline, post-treatment, and as absolute change (delta).
All values are reported as mean ± standard deviation (SD), together with median and full observed range (minimum–maximum).

Functional Outcomes

Baseline BCVA (LogMAR pre)

Müller+ Group
In CRVO eyes (n = 27), baseline BCVA showed:

- Mean: 0.789 ± 0.375
- Median: 1.0
- Range: 0.2–1.3

In BRVO eyes (n = 43):

- Mean: 0.463 ± 0.260
- Median: 0.4
- Range: 0.1–1.3

The dispersion of baseline BCVA values was greater in CRVO compared to BRVO eyes within the Müller+ group, as reflected by the higher standard deviation.

Müller− Group
In CRVO eyes (n = 6):

- Mean: 1.0 ± 0.19
- Median: 1.0
- Range: 0.7–1.3

In BRVO eyes (n = 6):

- Mean: 0.667 ± 0.418
- Median: 0.55
- Range: 0.2–1.3

The BRVO subgroup in the Müller− group demonstrated broader variability, as indicated by a higher SD relative to CRVO.

Post-Treatment BCVA (LogMAR post)

Müller+ Group

CRVO (n = 27):

- Mean: 0.493 ± 0.372
- Median: 0.5
- Range: 0–1.3

BRVO (n = 43):

- Mean: 0.298 ± 0.228
- Median: 0.2
- Range: 0–1.0

Post-treatment BCVA values demonstrated a shift toward lower LogMAR values in both subgroups compared to baseline.

Müller− Group

CRVO (n = 6):

- Mean: 0.717 ± 0.248
- Median: 0.7
- Range: 0.4–1.0

BRVO (n = 6):

- Mean: 0.400 ± 0.179
- Median: 0.35
- Range: 0.2–0.7

The post-treatment distribution appeared narrower compared to baseline values in all strata.

BCVA Change (LogMAR Delta)

Müller+ Group

CRVO (n = 27):

- Mean: 0.293 ± 0.292
- Median: 0.3
- Range: 0–1.1

BRVO (n = 43):

- Mean: 0.170 ± 0.235
- Median: 0.1
- Range: −0.3–1.1

The OVBR subgroup included negative delta values, indicating variability in direction of change.

Müller− Group

CRVO (n = 6):

- Mean: 0.283 ± 0.248
- Median: 0.3
- Range: 0–0.6

BRVO (n = 6):

- Mean: 0.267 ± 0.242
- Median: 0.2
- Range: 0–0.6

The magnitude of variation in LogMAR delta was smaller in Müller− subgroups compared to Müller+ OVCR.

Anatomical Outcomes

Baseline Central Retinal Thickness (CRT pre)

Müller+ Group

CRVO (n = 27):

- Mean: 673.5 ± 228.1 µm

- Median: 614 µm
- Range: 352–1239 µm

BRVO (n = 43):

- Mean: 517.0 ± 146.9 µm
- Median: 465 µm
- Range: 300–913 µm

The CRVO subgroup showed broader dispersion and higher maximal values compared to BRVO.

Müller− Group

CRVO (n = 6):

- Mean: 855.2 ± 241.7 µm
- Median: 873.5 µm
- Range: 570–1132 µm

BRVO (n = 6):

- Mean: 466.2 ± 72.0 µm
- Median: 430 µm
- Range: 423–605 µm

The CRVO Müller− subgroup demonstrated the highest baseline mean and median CRT values across all groups.

Post-Treatment CRT (CRT post)

Müller+ Group

CRVO (n = 27):

- Mean: 306.9 ± 85.5 µm
- Median: 290 µm
- Range: 216–637 µm

BRVO (n = 43):

- Mean: 267.4 ± 33.9 µm
- Median: 265 µm
- Range: 210–373 µm

Post-treatment CRT values were distributed within a narrower interval compared to baseline.

Müller− Group

CRVO (n = 6):

- Mean: 253.3 ± 44.2 µm
- Median: 250.5 µm
- Range: 188–326 µm

BRVO (n = 6):

- Mean: 351.8 ± 94.0 µm
- Median: 356.5 µm
- Range: 242–515 µm

Variability in post-treatment CRT was greater in the OVBR Müller− subgroup compared to OVCR Müller−.

CRT Change (CRT delta)

Müller+ Group

CRVO (n = 27):

- Mean: 366.6 ± 241.5 µm
- Median: 302 µm
- Range: 11–981 µm

BRVO (n = 43):

- Mean: 249.7 ± 156.3 µm
- Median: 206 µm
- Range: 19–686 µm

The CRVO subgroup exhibited wider dispersion and higher maximum delta values.

Müller− Group

CRVO (n = 6):

- Mean: 601.8 ± 237.2 µm
- Median: 644 µm
- Range: 309–877 µm

BRVO (n = 6):

- Mean: 114.3 ± 69.4 µm
- Median: 82 µm
- Range: 63–243 µm

The CRVO Müller– subgroup showed the highest median delta CRT

Analysis of Müller Cell Cone Status and Structural Disruption

A total of 33 CRVO eyes were included in the categorical analysis evaluating the association between Müller cell cone status and outer retinal disruption (ELM/IS–OS).
Overall, structural disruption was detected in 15 of 33 eyes (45.5%; 95% CI: 29.8–62.0%), while 18 eyes (54.5%) showed no disruption.
Among the 6 Müller-negative eyes, disruption was observed in 5 cases (83.3%; 95% CI: 43.6–97.0%), whereas 1 eye (16.7%) did not demonstrate disruption.
In the Müller-positive group (n = 27), disruption was present in 10 eyes (37.0%; 95% CI: 21.5–55.8%), while 17 eyes (63.0%) showed preserved outer retinal structure.

A total of 49 BRVO eyes were included in the categorical analysis evaluating the association of outer retinal disruption a (ELM/IS-OS) according to Müller cell cone status.
Overall, structural disruption of the ELM/IS–OS complex was detected in 6 of 49 eyes (12.2%; 95% CI: 5.7–24.2%), whereas 43 eyes (87.8%) demonstrated preserved outer retinal integrity.
Among the 6 Müller-negative eyes, disruption was observed in 3 cases (50.0%; 95% CI: 18.8–81.2%), while the remaining 3 eyes (50.0%) showed preserved structure.
In contrast, within the Müller-positive group (n = 43), disruption was present in 3 eyes (7.0%; 95% CI: 2.4–18.6%), whereas 40 eyes (93.0%) exhibited preserved ELM/IS–OS integrity.

CRVO - MCC integrity and central retinal thickness analysis

The study cohort was stratified according to the presence (Müller+) or absence (Müller−) of Müller cell cone alteration on structural OCT. The Müller+ group included 27 eyes, whereas the Müller− group comprised 6 eyes.

Three quantitative OCT-derived variables were analyzed:

1. Baseline central retinal thickness (CRT-pre)
2. Post-treatment central retinal thickness (CRT-post)
3. Absolute change in thickness following treatment (ΔCRT)

All variables were treated as continuous measures and compared between groups using the Brunner–Munzel test.

Baseline Central Retinal Thickness (CRT-pre)

Baseline CRT values in the Müller+ group ranged from 352 µm to 1239 µm, whereas in the Müller− group they ranged from 570 µm to 1132 µm.

Between-group comparison using the Brunner–Munzel test did not reveal a statistically significant difference (BM statistic = 1.85, $p = 0.124$).

The stochastic superiority effect size was 0.35. This indicates that, when randomly selecting one eye from each group, the probability that the Müller+ eye presents a higher baseline CRT than the Müller− eye is 35%.

Post-Treatment Central Retinal Thickness (CRT-post)

Post-treatment CRT values in the Müller+ group ranged from 216 µm to 637 µm, while in the Müller− group they ranged from 188 µm to 326 µm.

The Brunner–Munzel test did not demonstrate a statistically significant difference between groups (BM statistic = −1.45, $p = 0.205$).

The stochastic superiority effect size was 0.60, corresponding to a 60% probability that a randomly selected Müller+ eye shows a higher post-treatment CRT compared to a Müller− eye.

Absolute Thickness Change (ΔCRT)

The absolute change in retinal thickness (ΔCRT) in the Müller+ group ranged from 11 µm to 981 µm. In the Müller− group, ΔCRT values ranged from 309 µm to 877 µm.

The Brunner–Munzel test identified a statistically significant difference between groups (BM statistic = 3.04, $p = 0.013$).

The stochastic superiority effect size was 0.85. This indicates that, in 85% of randomly paired comparisons between groups, the Müller+ eye exhibited a greater thickness change than the Müller− eye.

CRVO - Comparison of Visual Acuity According to Müller Cell Cone Status

The study population was stratified according to the presence (Müller+) or absence/alteration (Müller−) of Müller cell cone. A total of 27 eyes were included in the Müller+ group and 6 eyes in the Müller− group.
Best-corrected visual acuity (BCVA), expressed in LogMAR units, was analyzed at baseline, after treatment, and as absolute change (delta). Between-group comparisons were performed using the Brunner–Munzel test, and the stochastic superiority effect size was calculated for each parameter.

Baseline Visual Acuity (LogMAR Pre)

At baseline, no statistically significant difference in BCVA was detected between the Müller+ and Müller− groups (Brunner–Munzel statistic = 1.67; $p = 0.111$).
The stochastic superiority effect size was 0.346. This indicates a 34.6% probability that a randomly selected eye from the Müller+ group had a higher LogMAR value compared to a randomly selected eye from the Müller− group.

Post-Treatment Visual Acuity (LogMAR Post)

Post-treatment BCVA did not differ significantly between groups (Brunner–Munzel statistic = 2.04; $p = 0.060$).
The stochastic superiority effect size was 0.299, corresponding to a 29.9% probability that a randomly selected Müller+ eye presented a higher post-treatment LogMAR value compared to a Müller− eye.

Visual Acuity Change (LogMAR Delta)

Analysis of the absolute change in BCVA (LogMAR delta) revealed no statistically significant difference between Müller+ and Müller− groups (Brunner–Munzel statistic = 0.153; $p = 0.883$).
The stochastic superiority effect size was 0.478, indicating a 47.8% probability that a randomly selected eye in the Müller+ group exhibited a greater LogMAR change compared to an eye in the Müller− group.

CRVO - Association Between Müller Cell Cone Alteration and Structural Disruption

To investigate the relationship between Müller cell cone status and the presence of structural disruption of ELM and IZ-EZ, a categorical analysis was performed using a contingency table approach.
A total of 33 eyes were included in this analysis. The distribution of cases according to Müller cell cone status and disruption is reported below:

	Disruption Present	**Disruption Absent**	**Total**
Müller −	5	1	6
Müller +	10	17	27
Total	15	18	33

Structural disruption was observed in 5 of 6 Müller-negative eyes (83.3%) and in 10 of 27 Müller-positive eyes (37.0%).

The association between Müller cell cone status and structural disruption was analyzed using Barnard's exact test.

The analysis yielded:

- Test statistic = 2.06
- Two-sided $p = 0.043$

Using this unconditional exact approach, the association reached statistical significance at the predefined threshold of $p < 0.05$.
The odds ratio derived from the contingency table was 8.50, indicating a substantially higher odds of outer retinal disruption in the Müller-negative group compared with the Müller-positive group.

BRVO - MCC integrity and central retinal thickness analysis

The BRVO subgroup included 49 eyes, stratified according to Müller cell cone status:

- Müller cell cone integrity (Müller+): n = 43
- Müller cell cone disruption (Müller−): n = 6

Three continuous anatomical variables were analyzed:

- Baseline central retinal thickness (CRT pre)
- Post-treatment central retinal thickness (CRT post)
- Absolute change in thickness (CRT delta)

Between-group comparisons were performed using the Brunner–Munzel test, given the unequal sample sizes and the absence of homoscedasticity assumptions. The stochastic superiority effect size was calculated for each comparison.

Baseline Central Retinal Thickness (CRT Pre)

The Brunner–Munzel test did not demonstrate a statistically significant difference in baseline CRT between Müller+ and Müller− groups (BM statistic = −0.95;p = 0.353). The stochastic superiority effect size was 0.587.

This indicates a 58.7% probability that a randomly selected Müller-positive eye had a higher baseline CRT compared to a Müller-negative eye.

Post-Treatment Central Retinal Thickness (CRT Post)

For post-treatment CRT, the Brunner–Munzel did not showed association (BM statistic = 2.38; p = 0.059)

The difference did not reach the predefined threshold for statistical significance (p < 0.05), although a trend toward between-group difference was observed.

The stochastic superiority effect size was 0.198. This corresponds to a 19.8% probability that a randomly selected Müller-positive eye exhibited a higher post-treatment CRT compared to a Müller-negative eye.

Absolute Thickness Change (CRT Delta)

Analysis of CRT delta revealed a statistically significant difference between groups:

- BM statistic = −3.33
- $p = 0.011$

The stochastic superiority effect size was 0.800. This indicates an 80.0% probability that a randomly selected Müller-positive eye demonstrated a greater thickness change compared to a Müller-negative eye.

BRVO – Visual Acuity According to Müller Cell Cone Status

The BRVO cohort included 49 eyes, of which 43 were classified as Müller-positive and 6 as Müller-negative. Best-corrected visual acuity (BCVA), expressed in LogMAR units, was evaluated at baseline, after treatment, and as absolute change (delta). Between-group comparisons were conducted using the Brunner–Munzel test.

Baseline visual acuity (LogMAR pre)

At baseline, visual acuity did not differ significantly between the two groups. The Brunner–Munzel statistic was 0.97 with a corresponding two-sided *p*-value of 0.370. The stochastic superiority index was 0.360, indicating a 36.0% probability that a randomly selected Müller-positive eye presented a higher baseline LogMAR value compared with a Müller-negative eye. The distribution of baseline values demonstrated substantial overlap between groups.

Post-Treatment Visual Acuity (LogMAR Post)

Post-treatment visual acuity similarly did not show a statistically significant difference between Müller-positive and Müller-negative eyes. The Brunner–Munzel test yielded a statistic of 1.77 with a *p*-value of 0.108. Although the test statistic suggested some separation in the distributions, the difference did not reach the predefined significance threshold. The corresponding stochastic superiority effect size was 0.328, reflecting a 32.8% probability that a randomly

selected Müller-positive eye exhibited a higher post-treatment LogMAR value compared with a Müller-negative eye.

Visual Acuity Change (LogMAR Delta)

Analysis of the absolute change in visual acuity (LogMAR delta) also failed to demonstrate a statistically significant between-group difference. The Brunner–Munzel statistic was 0.74 with a p-value of 0.490. The stochastic superiority index was 0.395, indicating a 39.5% probability that a randomly selected Müller-positive eye showed a greater change in LogMAR compared with a Müller-negative eye. The distribution of delta values overlapped considerably across groups, with no evidence of systematic dominance.

Overall, within the BRVO subgroup, no statistically significant differences in functional outcomes were observed according to Müller cell cone status. The estimated effect sizes were small, and the probabilistic indices did not indicate a consistent directional pattern between groups. All statistical tests were two-sided, and statistical significance was defined a priori as $p < 0.05$.

BRVO - Association Between Müller Cell Cone Alteration and Structural Disruption

A total of 49 eyes were included in the categorical analysis assessing the association between Müller cell cone status and outer retinal disruption involving the external limiting membrane and the interdigitation/ellipsoid zone (ELM/IZ–EZ).

The distribution of cases was as follows:

	Disruption Present	Disruption Absent	Total
Müller −	3	3	6
Müller +	3	40	43
Total	6	43	49

Structural disruption was observed in 3 of 6 Müller-negative eyes (50.0%), compared to 3 of 43 Müller-positive eyes (7.0%). Most Müller-positive eyes (93.0%) demonstrated preserved outer retinal structure.

Given the small size of the Müller-negative subgroup and the imbalance between categories, the association was evaluated using Barnard's exact test, an unconditional exact test for 2×2 contingency tables.

The analysis yielded:

- Test statistic = 3.01
- Two-sided p = 0.0074

Using this exact approach, the association between Müller cell cone status and structural disruption was statistically significant at the predefined significance threshold ($p < 0.05$).
The odds ratio derived from the contingency table was 13.33, indicating a substantially higher odds of outer retinal disruption in the Müller-negative group compared with the Müller-positive group.

Discussion

When restricting the analysis to statistically significant results emerging from our dataset, two elements deserve particular attention:

- the significantly greater **ΔCRT reduction** in the group with preserved Müller cell cone (Müller+),
- the higher prevalence and/or recovery of **ELM and IZ/EZ integrity** in the same group after the loading phase of anti-VEGF therapy.

In our cohort, visual acuity gains after three injections were overall modest and did not differ dramatically between groups. This finding should not be interpreted as unexpected. Functional recovery in retinal vein occlusion (RVO) is influenced by multiple variables beyond fluid resolution, including baseline ischemic burden, duration of edema, inner retinal disorganization (DRIL), and the pre-treatment condition of photoreceptors not considered in our study at baseline. Tsang et al. demonstrated that baseline disruption of ELM and EZ is strongly associated with worse visual acuity over time, and that although improvement in these bands increases the probability of visual gain, visual recovery remains multifactorial and not exclusively dependent on thickness reduction[34]
Therefore, the absence of large visual gains in our short-term analysis is consistent with existing evidence: early anti-VEGF–induced anatomical recovery does not invariably translate into immediate, proportional functional improvement. Visual acuity reflects the integrated performance of the neurovascular and neuroglial retina, not merely the degree of extracellular fluid.

Conversely, the statistically significant greater ΔCRT observed in the Müller+ group represents a robust structural signal. Eyes with preserved Müller cell cone architecture demonstrated a more pronounced reduction in central retinal thickness after the loading phase, indicating more efficient resolution of macular edema.

This finding is biologically coherent with the well-established role of Müller cells in retinal fluid regulation[34]. Müller cells are central to potassium siphoning, water transport, and maintenance of extracellular osmotic balance through channel systems such as Kir channels and aquaporins; dysfunction of these mechanisms contributes to intracellular swelling and extracellular cyst formation. When Müller cell structure is preserved—reflected in our study by intact Müller cell cone morphology—the retina likely retains a higher capacity to restore hydrostatic and ionic equilibrium once VEGF-driven vascular permeability is pharmacologically suppressed.

The foveal eversion (FE) literature further reinforces this interpretation. Arrigo et al. showed that FE—considered a surrogate marker of advanced Müller cell impairment—is associated with persistent macular edema and poorer anatomical outcomes in RVO[45]. In diabetic macular edema, FE similarly correlated with higher edema persistence and worse response profiles[55]. Within this conceptual framework, the Müller+ phenotype in our cohort can be interpreted as the structural opposite of FE: a retina in which the glial scaffold remains functionally competent, thereby facilitating fluid reabsorption after VEGF blockade. The greater ΔCRT reduction in Müller+ eyes is therefore not merely a statistical difference but a pathophysiologically meaningful signal of preserved glial-mediated homeostasis.

Integrity of ELM and IZ/EZ in Müller+: structural coherence of the neuroglial–photoreceptor unit

The second statistically significant finding—the higher integrity or recovery of ELM and IZ/EZ bands in the Müller+ group—further strengthens the interpretation of Müller cells as central modulators of anatomical recovery.

The external limiting membrane (ELM) represents the junctional complex between photoreceptors and Müller cells; its integrity depends directly on preserved Müller–photoreceptor interactions. The ellipsoid zone (EZ) and interdigitation zone (IZ) reflect photoreceptor inner segment mitochondrial integrity and photoreceptor–RPE interaction, respectively. Tsang et al. demonstrated that baseline and longitudinal integrity of ELM and EZ are

strongly associated with better visual prognosis and with improved response to anti-VEGF therapy in RVO[34]

In our dataset, the association between Müller cell cone preservation and greater integrity of these outer retinal bands suggests that when the Müller scaffold is intact, the outer retina is structurally more resilient. This is consistent with the biological role of Müller cells in metabolic support, trophic signaling, and structural stabilization of photoreceptors[44]. By maintaining extracellular homeostasis and structural alignment, preserved Müller cells likely protect or facilitate restoration of ELM and IZ/EZ continuity during edema resolution.
Conversely, disruption of this glial support system may predispose to outer retinal disorganization, even if fluid is pharmacologically reduced.
Importantly, the FE studies also report higher rates of DRIL and outer retinal disruption in eyes with FE, reinforcing the idea that advanced Müller dysfunction is accompanied by broader architectural disorganization. In contrast, the Müller+ group in our study appears characterized by a structurally coherent outer retina, capable of anatomical recovery once vascular leakage is controlled.

Taken together, our statistically significant findings support a coherent mechanistic model:

- Visual acuity gains were modest, which is consistent with the multifactorial determinants of functional recovery in RVO.
- ΔCRT reduction was significantly greater in Müller+ eyes, indicating superior edema resolution.
- ELM and IZ/EZ integrity was better preserved or restored in Müller+ eyes, reflecting maintained neuroglial–photoreceptor structural integrity.

These results suggest that anti-VEGF therapy addresses the vascular permeability component of macular edema, but the magnitude of anatomical recovery depends critically on the pre-existing competence of the Müller cell system. When Müller cell architecture is preserved, the retina retains the intrinsic capacity to re-establish tissue homeostasis and outer retinal

organization, leading to greater fluid resolution and structural normalization—even if short-term visual gains remain limited due to additional pathogenic factors.

Thus, our findings position the Müller cell cone not merely as a descriptive OCT feature, but as a potential functionally meaningful biomarker of retinal resilience and treatment responsiveness in RVO-related macular edema.

Conclusions

The present study investigated the role of Müller cell cone integrity as a structural biomarker in retinal vein occlusion (RVO)–related macular edema, with particular attention to its association with central retinal thickness reduction (ΔCRT) and outer retinal band integrity (ELM and IZ/EZ) following a loading phase of anti-VEGF therapy.

Our findings demonstrate that eyes with preserved Müller cell cone architecture exhibited a significantly greater reduction in central retinal thickness and a higher prevalence of preserved or restored ELM and IZ/EZ integrity after treatment. Conversely, visual acuity gains were modest and did not differ substantially between groups in the short term.

These results support a biologically coherent interpretation: anti-VEGF therapy primarily addresses vascular permeability and exudation, but the magnitude of anatomical recovery appears to depend on the intrinsic homeostatic competence of the retinal tissue. Müller cells play a central role in retinal water transport, ion buffering, and structural stabilization of the fovea. When their architecture is preserved, the retina appears more capable of re-establishing hydrostatic equilibrium once VEGF-driven leakage is suppressed. This may explain the significantly greater ΔCRT observed in Müller+ eyes.

Moreover, the association between Müller cell cone preservation and outer retinal band integrity is structurally meaningful. The external limiting membrane (ELM) represents the junctional interface between Müller cells and photoreceptors, and the ellipsoid/interdigitation zones reflect photoreceptor structural integrity.
The preservation of these bands in Müller+ eyes suggests that intact glial scaffolding may contribute to maintaining photoreceptor alignment and metabolic support, facilitating structural restoration even when functional recovery remains limited in the short term.

Importantly, the modest visual acuity gains observed in our cohort are consistent with existing literature indicating that most OCT biomarkers show limited independent prognostic strength and that visual recovery in RVO is multifactorial. Functional outcomes are influenced not only by edema resolution and outer retinal integrity, but also by ischemic burden, inner retinal disorganization, baseline visual acuity, and disease chronicity.

Limitations

Several limitations inherent to the observational design of this study must be acknowledged.

First, as a retrospective observational analysis, the study is subject to selection bias and confounding. Although statistically significant associations were identified for ΔCRT and outer retinal integrity, causality cannot be established. The absence of randomized allocation prevents exclusion of baseline differences between groups that may have influenced anatomical response.

Second, the sample size, while sufficient to detect certain statistically significant differences, limits statistical power—particularly for functional endpoints.

Third, biomarker assessment was based on structural OCT analysis without centralized reading center adjudication. As highlighted in the systematic review by Hatamnejad et al., heterogeneity in biomarker definitions and assessment methodologies significantly reduces certainty of evidence in the literature[44]. Standardization of definitions—particularly for Müller cell cone alteration, ELM/EZ integrity grading, and retinal thickness measurement—is essential to improve reproducibility and external validity.

Fourth, the relatively short follow-up limited evaluation of long-term functional implications. Outer retinal recovery may precede measurable visual gain, and longer observation periods could better clarify the relationship between structural restoration and functional improvement.

Finally, multivariable modeling was limited by sample size and available covariates. Given the coexistence of multiple OCT biomarkers in RVO, future analyses should incorporate comprehensive multivariate approaches to determine the independent prognostic value of Müller cell cone integrity relative to other structural parameters.

Future perspectives

The findings of this study provide a rationale for a prospective, adequately powered investigation with standardized imaging and reporting protocols. Such a study should include:

- Predefined and validated criteria for Müller cell cone alteration.
- Centralized reading center evaluation of OCT biomarkers.
- Uniform definitions for ELM, EZ, and IZ integrity.
- Multivariable statistical models adjusting for baseline visual acuity, ischemic status, and coexisting OCT features.

A prospective design would reduce bias, enhance statistical power, and allow more precise evaluation of the independent predictive value of Müller cell cone integrity. Additionally, longitudinal assessment beyond the loading phase would clarify whether early anatomical advantages in Müller+ eyes translate into superior long-term functional outcomes or reduced recurrence rates.

Final considerations

In conclusion, this study suggests that preservation of the Müller cell cone is associated with superior anatomical response and greater maintenance of outer retinal structural integrity following anti-VEGF therapy in RVO-related macular edema. Although short-term visual gains remain limited and multifactorial, Müller cell cone integrity may represent a biologically meaningful biomarker of retinal resilience.

Future prospective, standardized, and adequately powered studies are necessary to validate these findings and to establish whether Müller cell–centered biomarkers can be reliably integrated into prognostic stratification and personalized therapeutic algorithms in retinal vein occlusion.

Chapter 3

Validation of smartphone based telemedicine tools in ophthalmology

Introduction

Telemedicine has progressively transformed the delivery of healthcare by enabling the remote acquisition, transmission, and interpretation of clinical data. In ophthalmology, this paradigm—commonly referred to as teleophthalmology—has gained increasing relevance in response to the growing global burden of chronic eye diseases, particularly those affecting the retina. Age-related macular degeneration (AMD), diabetic retinopathy (DR), retinal vein occlusion (RVO), and other macular disorders represent leading causes of visual impairment worldwide and require long-term monitoring, repeated functional testing, and timely therapeutic intervention to prevent irreversible vision loss. The demographic shift toward an aging population, combined with the limited availability of retinal specialists in certain geographic areas, has further highlighted the need for innovative and scalable models of care delivery.

One of the earliest and most extensively validated applications of teleophthalmology is the screening and monitoring of diabetic retinopathy through store-and-forward systems based on digital fundus photography. Large-scale telemedicine programs using non-mydriatic fundus cameras in primary care settings, with remote grading by trained readers or ophthalmologists, have demonstrated high diagnostic accuracy and clinical effectiveness. A systematic review and meta-analysis by Kawaguchi et al. reported that teleophthalmology screening for DR and AMD achieves sensitivity and specificity comparable to in-person examinations, supporting its role as a reliable alternative in screening contexts[56]. More recently, the American Academy of Ophthalmology reaffirmed that telemedicine-based DR screening improves adherence to recommended screening intervals and facilitates early detection of sight-threatening disease[57]. Economic analyses have further demonstrated that teleophthalmology screening strategies can be cost-effective, particularly when implemented in populations with limited access to specialized care[58].

Beyond diabetic retinopathy, teleophthalmology models have been successfully implemented in glaucoma care, where community-based data acquisition—such as optic disc photography and visual field testing—can be transmitted electronically for remote consultant review. The Cambridge Community Optometry Glaucoma Scheme demonstrated that structured telemedical pathways can safely triage and monitor glaucoma patients, reducing the burden on hospital eye services while maintaining clinical safety[59]. Similar experiences in other healthcare systems have confirmed the feasibility of remote optic nerve evaluation and risk stratification[60]. These models highlight the capacity of teleophthalmology not only as a screening tool but also as an integrated component of chronic disease management.

In the field of macular diseases, telemedicine has expanded toward home-based functional monitoring aimed at detecting early disease progression. The Home Monitoring of the Eye (HOME) Study evaluated a home telemonitoring system for patients at high risk of neovascular AMD and demonstrated that remote self-testing can be effectively incorporated into clinical pathways for earlier detection of choroidal neovascularization[61,62]. Early identification of functional deterioration is particularly relevant in macular disorders, where delays in recognition of disease reactivation may compromise visual outcomes. These findings support the concept that telemonitoring systems can complement standard follow-up and improve responsiveness to disease progression.

The rapid evolution of mobile technologies has further broadened the scope of teleophthalmology. Smartphone-based visual function testing has emerged as a practical and accessible solution for remote assessment. Bastawrous et al. developed and validated a smartphone-based visual acuity test (Peek Acuity), demonstrating good agreement with conventional logMAR charts and adequate repeatability for clinical and field use[63]. Subsequent validation studies have evaluated the accuracy and reliability of different visual acuity applications in teleophthalmology settings, confirming that, when standardized testing conditions are ensured, digital assessments can achieve clinically acceptable levels of agreement with traditional charts[64]. Importantly, these tools offer

advantages in terms of portability, scalability, and integration into digital health platforms.

Despite these promising developments, evidence remains limited regarding the application of smartphone-based visual acuity testing and digital Amsler grid assessment specifically in patients with established macular pathology. Macular diseases pose unique challenges, as central visual distortion and metamorphopsia may influence test performance differently from refractive or glaucomatous conditions.

Therefore, direct comparison between smartphone-derived psychophysical measurements and standard in-clinic assessments is essential to determine their clinical interchangeability and potential integration into structured telemedicine services.

Aim of the Study

Age-related macular degeneration, retinal vein occlusion, vitreomacular interface disorders, and diabetic retinopathy are chronic retinal diseases that are highly prevalent in the general population. After diagnosis and throughout the therapeutic pathway, patients must undergo regular follow-up visits and outpatient tests to monitor disease course.

Follow-up assessments typically include evaluation of distance and near visual acuity, the Amsler grid test, and instrumental investigations.

Two smartphone applications recently developed in Europe allow functional testing to be performed. Smart Optometry provides multiple tests, including the Amsler grid and near visual acuity measurement, whereas Peek Acuity Pro enables distance visual acuity assessment.

Although these applications have already been clinically tested, their use in the evaluation of patients with macular disorders has not yet been reported in the literature.

The aim of this study was to assess the agreement between measurements obtained with these applications and those obtained during routine in-person clinical assessment in a macular disease outpatient setting.

Materials and Methods

Between 1 and 9 September 2022, a cross-sectional study was conducted at the SC Ophthalmology Unit of the Ospedale di Circolo e Fondazione Macchi to compare the results of measurements obtained with smartphone applications for distance visual acuity, near visual acuity, and the Amsler test with those obtained during routine outpatient evaluation. A total of 69 eligible subjects were selected, corresponding to 98 eyes.

Inclusion criteria were:

- Age > 18 years
- Positive medical history for:
    - Macular pucker
    - Age-related macular degeneration
    - Retinal vein occlusion
    - Diabetic retinopathy
- Clear ocular media: pseudophakia or early cataract up to stage N2C2

Exclusion criteria were:

- Previous vitreoretinal surgery
- Media opacities, including:
    - Vitreous hemorrhage
    - Cataract stage > N2C2
    - Corneal opacities
- Visual acuity worse than 1.0 logMAR

Two smartphone applications available in Europe were used: Smart Optometry App (v. 3.4 full, Idrija, Slovenia) and Peek Acuity Pro (v. 3.5.13, London, UK). These allow psychophysical tests on smartphones and tablets comparable to those routinely used during in-person ophthalmic examinations. Smart Optometry offers several functional tests; for this study, the near visual acuity test and the Amsler grid test were selected. Peek Acuity Pro was chosen for distance visual acuity assessment.

For smartphone testing, a single device was used: Xiaomi Redmi Note 8 Pro with Android operating system (6.53-inch display, 2340 × 1080 pixel resolution, Android version 11.0). Routine outpatient tests included a 3-meter ETDRS chart, a paper Reduced Snellen near vision chart at 40 cm, and a paper Amsler grid. Eligible patients were informed about the rationale and procedures of the study and provided written informed consent. The study adhered to the principles of the Declaration of Helsinki and the ethical committee of the university hospital approved the study.

Peek Acuity Pro

Peek Acuity Pro is an application developed to assess distance visual acuity and is classified as a CE Class I medical device. It can be installed free of charge only on Android devices and is available exclusively in English. A step-by-step tutorial is provided, including a vision simulator. Assessment can be performed only with an optotype depicting tumbling “E” (Albini E). The test distance can be set at 2 or 3 meters, and the measurement scale can be selected among logMAR, Snellen (6/6), or Imperial (20/20). In this study, patients were positioned at 3 meters and results were recorded in logMAR.

The app displays one letter at a time: an “E” oriented at 0°, 90°, 180°, or 270°, surrounded by a square frame to simulate the crowding effect of standard optotypes. The patient indicates the orientation verbally or, preferably, by pointing with a finger; the operator then swipes on the screen in the indicated direction. During the study, the operator could not see whether each response was correct while looking at the screen. If the patient was unable to respond, the operator had to shake the smartphone until a new letter appeared, signaled by device vibration. Depending on the patient’s response, the app decreased or increased the optotype size. If the app detected visual acuity worse than 1.0 logMAR, the operator continued the test at 1 meter. If the patient responded correctly at this distance, the test ended with a score of 1.3 logMAR; otherwise, the test proceeded toward outcomes corresponding to counting fingers, hand motion, or light perception. At this stage, tumbling “E” optotypes were no longer displayed; instead, the patient was asked to identify the number of black

stripes shown on the screen. If correct, the result was recorded as counting fingers. If not, the test continued with a moving black square: if the patient detected the motion, the test ended as hand motion; otherwise, the final assessment was light perception. If the patient perceived the smartphone flashlight, the result was recorded as light perception; if not, no light perception.

The test always ended automatically with vibration and immediate display of the result in logMAR. For optimal performance, screen brightness was set to 100%, with no power-saving features or color alteration modes enabled.

Smart Optometry

Smart Optometry is a free application for Android and iOS devices that allows anyone to perform fifteen psychophysical tests, including near visual acuity and the Amsler grid. The language can be set among eleven options, including Italian. Before each test, instructions for correct execution are provided. Test results are not stored.

For near visual acuity, multiple near optotypes are available: tumbling “E” (Albini E), Landolt C, Arabic letters, and sentences. Values are expressed as decimals from 0.1 to 1. In this study, the smartphone was positioned at 40 cm from the patient’s eyes and the tumbling “E” optotype was selected. Decimal results were subsequently converted to logMAR. During the test, five letters were displayed per line and the patient was asked to identify their orientation by indicating with the hand from left to right. The operator verified correctness and advanced to the next line if at least three out of five “E” optotypes were correctly identified. The test ended either when the subject correctly identified at least three optotypes up to the 1.0 decimal line, or when fewer than three letters were recognized on a given line; in the latter case, the recorded result was the decimal value of the previous line.

The Amsler grid test was displayed with a white background, black grid lines, and a central black fixation point. The test was held at 40 cm from the patient’s

eyes, and the operator asked the patient to report any distortions of the lines while fixating the central point.

Data Collection

Data collection occurred in two separate sessions on the same day and was carried out by two different examiners who were unable to communicate the results to each other. The examiner performing the smartphone tests was not a healthcare professional, whereas routine outpatient tests were performed by an experienced ophthalmologist. All tests were conducted monocularly, with the best possible refractive correction.
In the first session, the patient underwent smartphone-based testing:

- Distance visual acuity with Peek Acuity Pro
- Near visual acuity with Smart Optometry
- Amsler grid test with Smart Optometry

In the second session, the patient underwent routine outpatient testing:

- Distance visual acuity with a 3-meter ETDRS chart
- Near visual acuity with a paper Reduced Snellen near vision chart (tumbling “E”) at 40 cm
- Paper Amsler grid test

Statistical Analysis

The three psychophysical tests were analyzed in Excel using two different statistical approaches.
For distance and near visual acuity, Bland–Altman plots were used, as this method is considered the most appropriate quantitative approach to evaluate agreement between two measurement systems [65]. The Bland–Altman plot is a scatter plot showing the relationship between the difference of the two measurements (measurement error) and their mean (the best estimate of the true value). The closer the difference is to zero, the better the agreement between the two systems.
The plot also includes:

- the bias line, corresponding to the mean difference between measurements.
- upper and lower limits of the 95% confidence interval (CI) of the bias.
- upper and lower limits of agreement, defined as the interval expected to contain 95% of samples in the population.

Two measurement methods are considered in agreement if differences fall within the limits of agreement. Moreover, if the equality line falls within the 95% CI of the bias, then the bias is not statistically significant. However, this alone is not sufficient to claim interchangeability between methods and a priori definition of the maximum clinically acceptable CI width is required. In this study, a clinically acceptable interval of 0.04 logMAR was defined. In Snellen chart, each line consists of five letters, each worth 0.02 logMAR; therefore, a full line corresponds to 0.1 logMAR (0.02 × 5). During testing, if the patient reads at least three out of five letters on a given line (0.06 logMAR), the next line can be attempted. Because at most two letters out of five can be missed, the clinically acceptable CI is the sum of the value of two incorrect letters, i.e., 0.04 logMAR (0.02 × 2).

For the Amsler grid test, a qualitative analysis was performed because the result could only be positive or negative. Cohen's kappa was calculated to evaluate the level of inter-rater agreement beyond chance between two qualitative assessments. Kappa can range up to 1. Agreement strength was interpreted according to the Landis and Koch (1977) classification: <0 no agreement; 0–0.20 slight; 0.21–0.40 fair; 0.41–0.60 moderate; 0.61–0.80 substantial; 0.81–1 almost perfect [66].

Results

A total of 69 subjects were enrolled: 36 males and 33 females, aged 39 to 83 years (mean 63.91 years). In 29 patients, both eyes were examined either because both met inclusion criteria or because one was healthy and the other met inclusion criteria.
Overall, 98 eyes were examined: 46 right eyes and 52 left eyes. Healthy and diseased eyes were 54 and 44, respectively. The pathological eyes presented the diseases reported in the table 1:

Pathology	Number of Eyes
Macular dystrophy	9
Dry AMD	4
Neovascular AMD	8
Diabetic macular edema	4
Vascular macular edema	5
Inflammatory macular edema	3
Macular pucker	4
Myopic maculopathy	4
Central serous chorioretinopathy	2
Amblyopia	1

Table 1 - List of diseases identified during data collection.

Regarding lens transparency: 27 eyes had a clear crystalline lens, 34 were pseudophakic, and 37 had early cataract not exceeding stage N2C2.
The spherical equivalent ranged from −7.00 to +4.00 diopters (mean +0.10): 25 eyes were myopic, 29 emmetropic, and 44 hyperopic.

Distance Visual Acuity
Distance visual acuity values obtained with Peek Acuity Pro ranged from 0.0 to 0.8 logMAR (mean 0.11 logMAR), whereas those obtained with the ETDRS chart ranged from 0.0 to 1.0 logMAR (mean 0.13 logMAR).

The Bland–Altman plot for distance visual acuity (Figure 1) showed a mean difference of −0.02 logMAR, corresponding to an average error of one letter. The 95% CI (−0.04 to 0.00 logMAR) included the equality line, and the limits of agreement included 95% of samples.

In healthy eyes, the mean difference was −0.01 logMAR, closer to zero than the overall sample. The 95% CI (−0.014 to 0.034 logMAR) included the equality line, and 91% of samples lay within the limits of agreement (Figure 2). The range of mean measurements was 0.0–0.15 logMAR. Values obtained with both Peek Acuity Pro and ETDRS were between 0.0 and 0.3 logMAR, with mean values of 0.0 and 0.1 logMAR, respectively. The average error was less than one letter.

In diseased eyes, the mean difference was −0.03 logMAR; the equality line was included in the 95% CI (−0.06 to 0.00 logMAR), and 95% of samples lay within the limits of agreement (Figure 3). The range of mean measurements was 0.0–0.85 logMAR. Peek Acuity Pro measurements ranged 0.0–0.8 logMAR, whereas chart measurements ranged 0.0–1.0 logMAR, with mean 0.2 logMAR in both methods. The average error corresponded to approximately one and a half letters.

Table 2 presents the data obtained from the analysis of measurements acquired with Peek Acuity Pro and the ETDRS chart.
In the first row, the results from the comparison of all 98 eyes are reported: the mean difference was −0.02 logMAR, the 95% confidence interval (CI) of the bias ranged from −0.04 to 0.00 logMAR, and the limits of agreement were between −0.20 and +0.16 logMAR.
In the second row, the results from the comparison within the healthy eye subgroup are shown: the mean difference was −0.01 logMAR, the 95% CI ranged from −0.014 to 0.034 logMAR, and the limits of agreement were between −0.18 and +0.16 logMAR.
In the final row, the comparison within the pathologic eye subgroup demonstrated a mean difference of −0.03 logMAR, a 95% CI of the bias ranging

from −0.06 to 0.00 logMAR, and limits of agreement between −0.22 and +0.16 logMAR.

Comparison (Peek -ETDRS)	N° Eyes	Mean Difference (logMAR)	95% CI of the Mean Difference (logMAR)	Limits of Agreement (logMAR)
Distance (All eyes)	98	-0.02	-0.02 ± 0.02	-0.20 to +0.16
Distance (Healthy eyes)	54	-0.01	0.01 ± 0.024	-0.18 to +0.16
Distance (Pathologic eyes)	44	-0.03	-0.03 ± 0.03	-0.22 to +0.16

Table 2 - Results obtained from the analysis of data collected during distance visual acuity testing. In the first row, the analysis includes all eyes; in the second row, only healthy eyes; and in the last row, only eyes with pathology. The mean difference corresponds to the standard error (bias). The 95% CI of the mean difference indicates the 95% confidence interval of the mean difference. The limits of agreement represent the lower and upper bounds of the agreement interval. The reported data were used to generate the Bland–Altman plots (Figures 1, 2, and 3).

The Bland–Altman plots shown below (Figures 1, 2, and 3) illustrate the comparison between Peek Acuity Pro and ETDRS measurements in all eyes, in the healthy eye subgroup, and in the pathologic eye subgroup, respectively. In all three plots, the bias line, the 95% confidence interval limits, and the limits of agreement are displayed.

In Figure 1, the equality line is included within the 95% confidence interval of the bias, and 93 out of 98 samples fall within the limits of agreement. In Figure 2, the equality line is included within the 95% confidence interval of the bias, and 49 out of 54 samples fall within the limits of agreement. In Figure 3, the equality line is included within the 95% confidence interval of the bias, and 42 out of 44 samples fall within the limits of agreement.

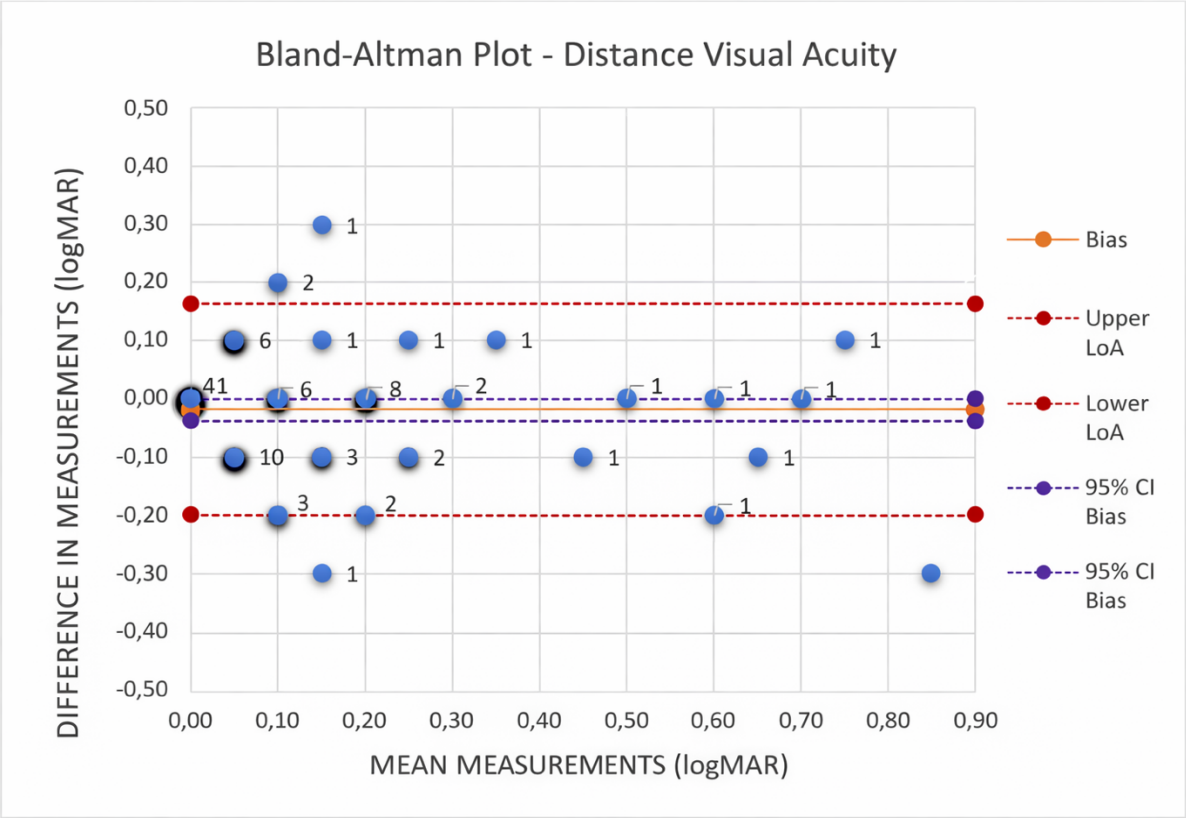

Figure 1 - Bland–Altman plot of agreement between Peek Acuity Pro and ETDRS in measuring distance visual acuity is evaluated. The bias line represents the mean difference between the two measurements. Upper LoA and Lower LoA correspond to the upper and lower limits of agreement, respectively. The two lines labeled as 95% CI of the bias indicate the upper and lower bounds of the 95% confidence interval of the mean difference.

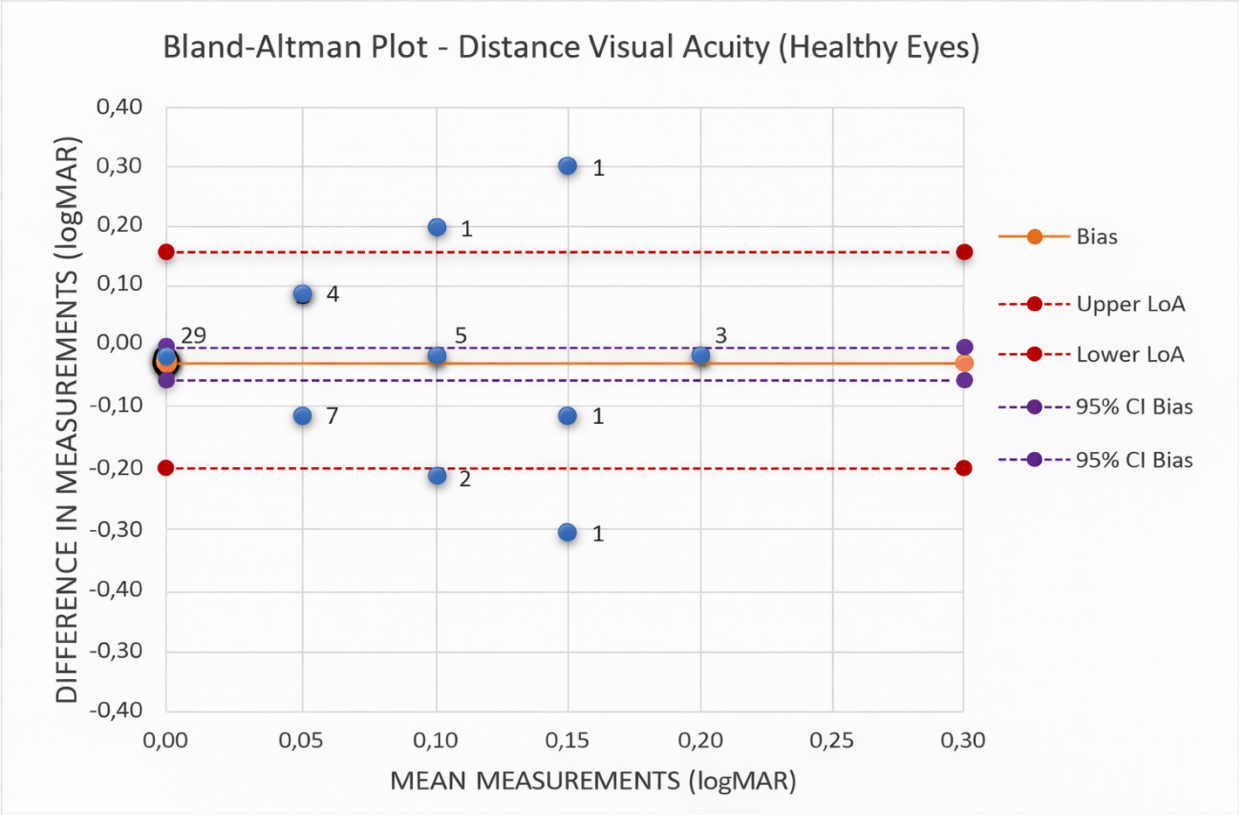

Figure 2 - This Bland–Altman plot illustrates the agreement between Peek Acuity and ETDRS in measuring distance visual acuity in healthy eyes. The bias line represents the mean difference between the two measurement methods. Upper LoA and Lower LoA indicate the upper and lower limits of agreement, respectively. The two lines labeled as 95% CI of the bias represent the upper and lower bounds of the 95% confidence interval of the mean difference.

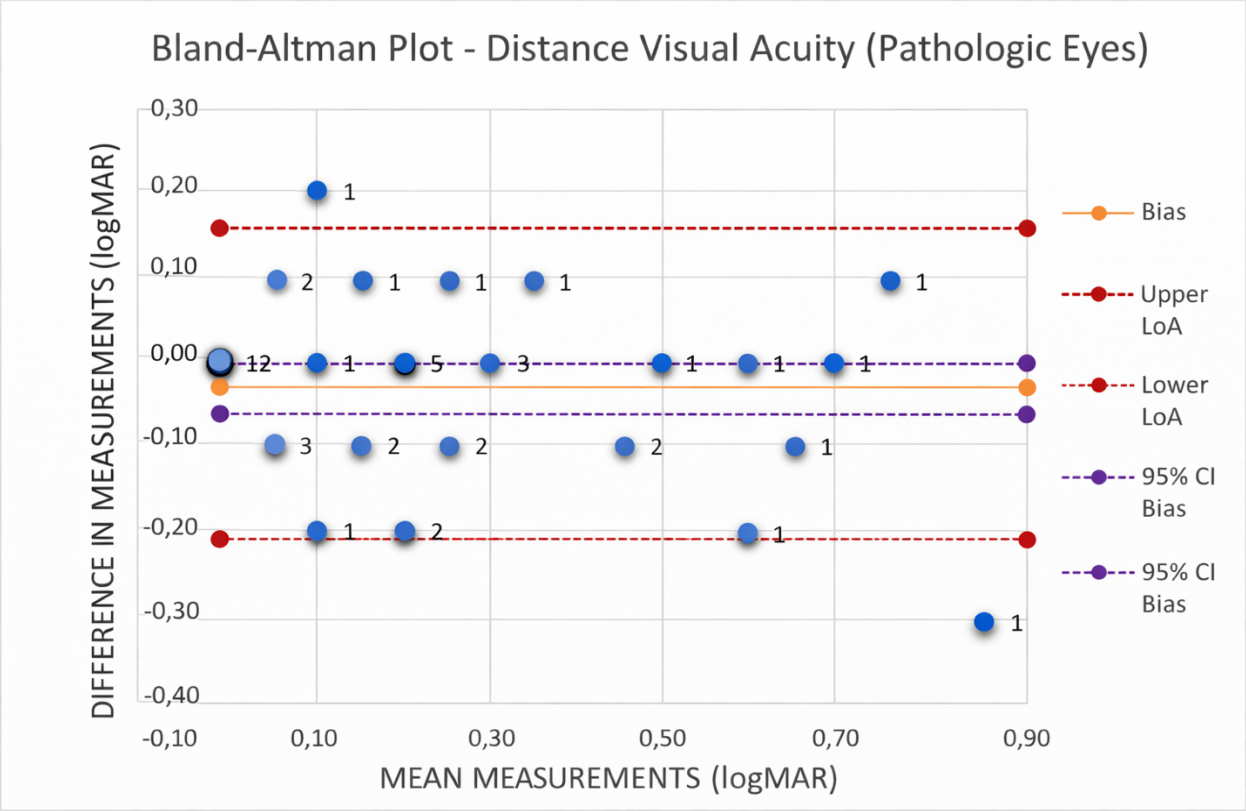

Figure 3 - This Bland–Altman plot illustrates the agreement between Peek Acuity and ETDRS in measuring distance visual acuity in pathologic eyes. The bias line represents the mean difference between the two measurement methods. Upper LoA and Lower LoA indicate the upper and lower limits of agreement, respectively. The two lines labeled as 95% CI of the bias represent the upper and lower bounds of the 95% confidence interval of the mean difference.

Near Visual Acuity

Near visual acuity values obtained with Smart Optometry ranged from 0.10 to 1.00 (decimal scale), with a mean of 0.75. Paper near acuity ranged from 0.20 to 1.0 (decimal scale), with a mean of 0.72. For statistical analysis, all values were converted to logMAR.

The mean difference between measurements was 0.0 logMAR; therefore, the standard error corresponded to zero letters. In the Bland–Altman plot, the bias line overlapped with the equality line. The 95% CI ranged from −0.018 to +0.018. Ninety-four percent of samples were within the limits of agreement.

For healthy eyes, the mean difference was −0.03 logMAR, with a 95% CI from −0.046 to −0.014 logMAR. Only 91% of samples were within the limits of agreement and none lay within the CI; 33 samples were on the zero line. Mean measurements ranged from 0.0 to 0.35 logMAR. Individually, Smart Optometry values ranged 0.0–0.4 logMAR (mean 0.1), while paper optotype values ranged 0.0–0.3 logMAR (mean 0.1). The standard error of −0.03 logMAR corresponds to about one and a half letters; thus, the two systems are interchangeable.

In diseased eyes, the mean difference was 0.03 logMAR, with a 95% CI from −0.063 to +0.003 logMAR. Ninety-three percent of samples were within the limits of agreement, with about half on the equality line. Mean measurements ranged from 0.0 to 0.85 logMAR. Smart Optometry values ranged 0.0–1.0 logMAR (mean 0.3), while paper near chart values ranged 0.1–0.7 logMAR (mean 0.3). The standard error of 0.03 logMAR corresponds to about one and a half letters.

Comparison (Smart Optometry –Snellen Chart)	**N° Eyes**	**Mean Difference (logMAR)**	**95% CI of the Mean Difference (logMAR)**	**Limits of Agreement (logMAR)**
Near (All eyes)	98	0.00	0.00 ± 0.018	-0.18 to +0.18
Near (Healthy eyes)	54	-0.03	-0.03 ± 0.016	-0.15 to +0.09
Near (Pathologic eyes)	44	0.03	0.03 ± 0.033	-0.19 to +0.25

Table 3 - near visual acuity agreement results for the overall sample and for healthy and diseased eye subgroups.

The Bland–Altman plots shown below (Figures 4, 5, and 6) illustrate the comparison between the near visual acuity measurements obtained with Smart Optometry and the Reduced Snellen near vision chart in all eyes, in the healthy eye subgroup, and in the pathologic eye subgroup, respectively.

In all three plots, the bias line, the 95% confidence interval limits, and the limits of agreement are displayed.

In Figure 4, the equality line coincides with the bias line, and 92 out of 98 samples fall within the limits of agreement. In Figure 5, the equality line is not included within the 95% confidence interval of the bias, and 49 out of 54 samples fall within the limits of agreement. In Figure 6, the equality line is included within the 95% confidence interval of the bias, and 41 out of 44 samples fall within the limits of agreement.

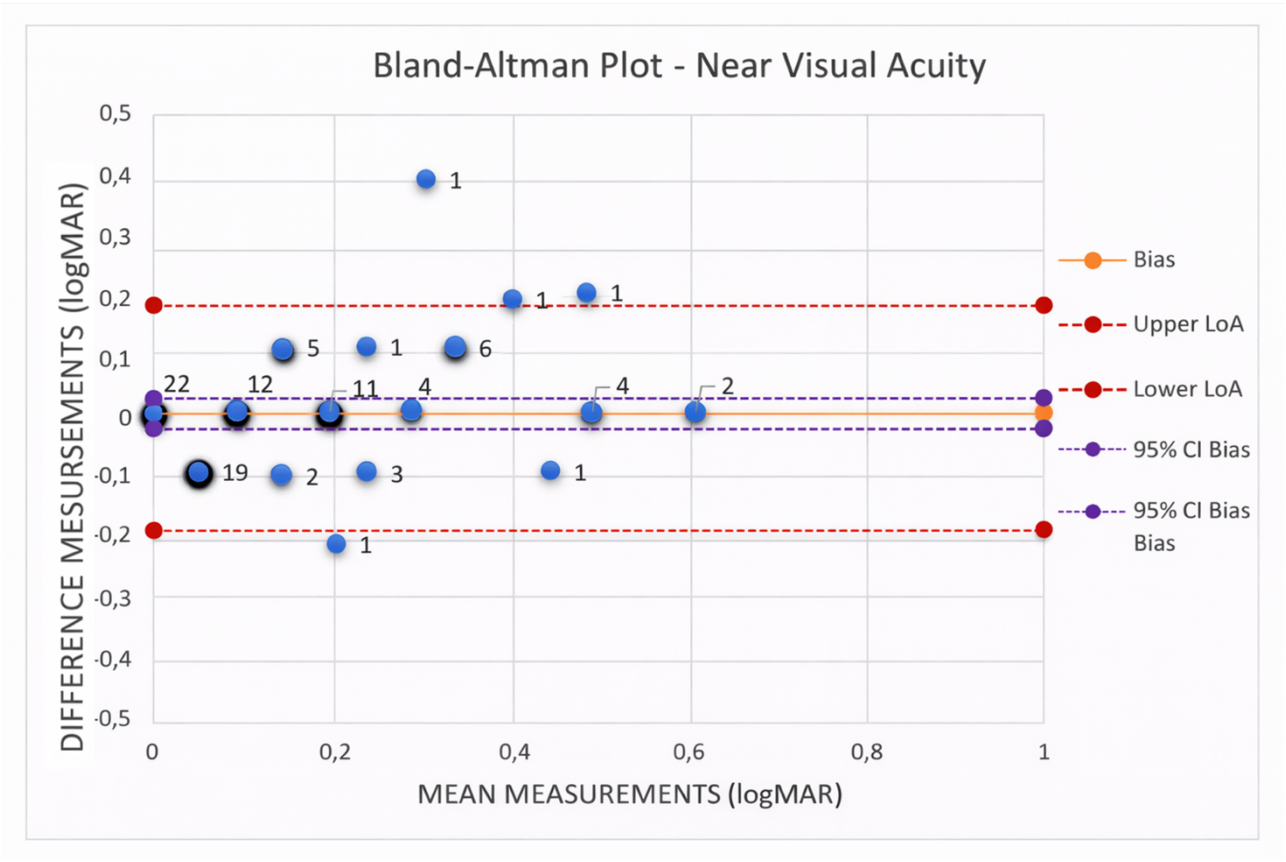

Figure 4 - In this Bland–Altman plot, the agreement between Smart Optometry and the Reduced Snellen near vision chart in measuring near visual acuity is evaluated. The bias line represents the mean difference between the two measurement methods. Upper LoA and Lower LoA correspond to the upper and lower limits of agreement, respectively. The two lines labeled as 95% CI of the bias represent the upper and lower bounds of the 95% confidence interval of the mean difference.

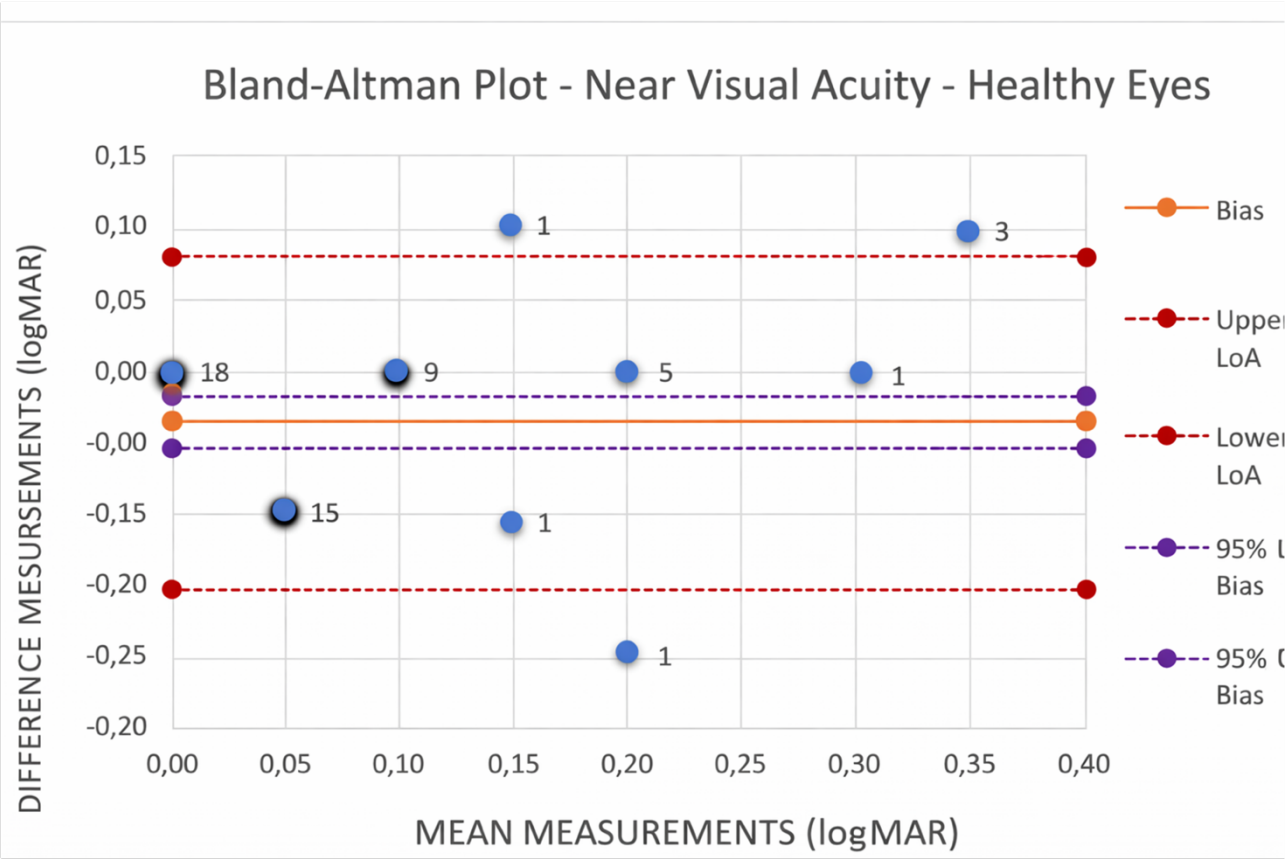

Figure 5 - In this Bland–Altman plot, the agreement between Smart Optometry and the Reduced Snellen near vision chart in measuring near visual acuity in healthy eyes is evaluated. The bias line represents the mean difference between the two measurement methods. Upper LoA and Lower LoA correspond to the upper and lower limits of agreement, respectively. The two lines labeled as 95% CI of the bias represent the upper and lower bounds of the 95% confidence interval of the mean difference.

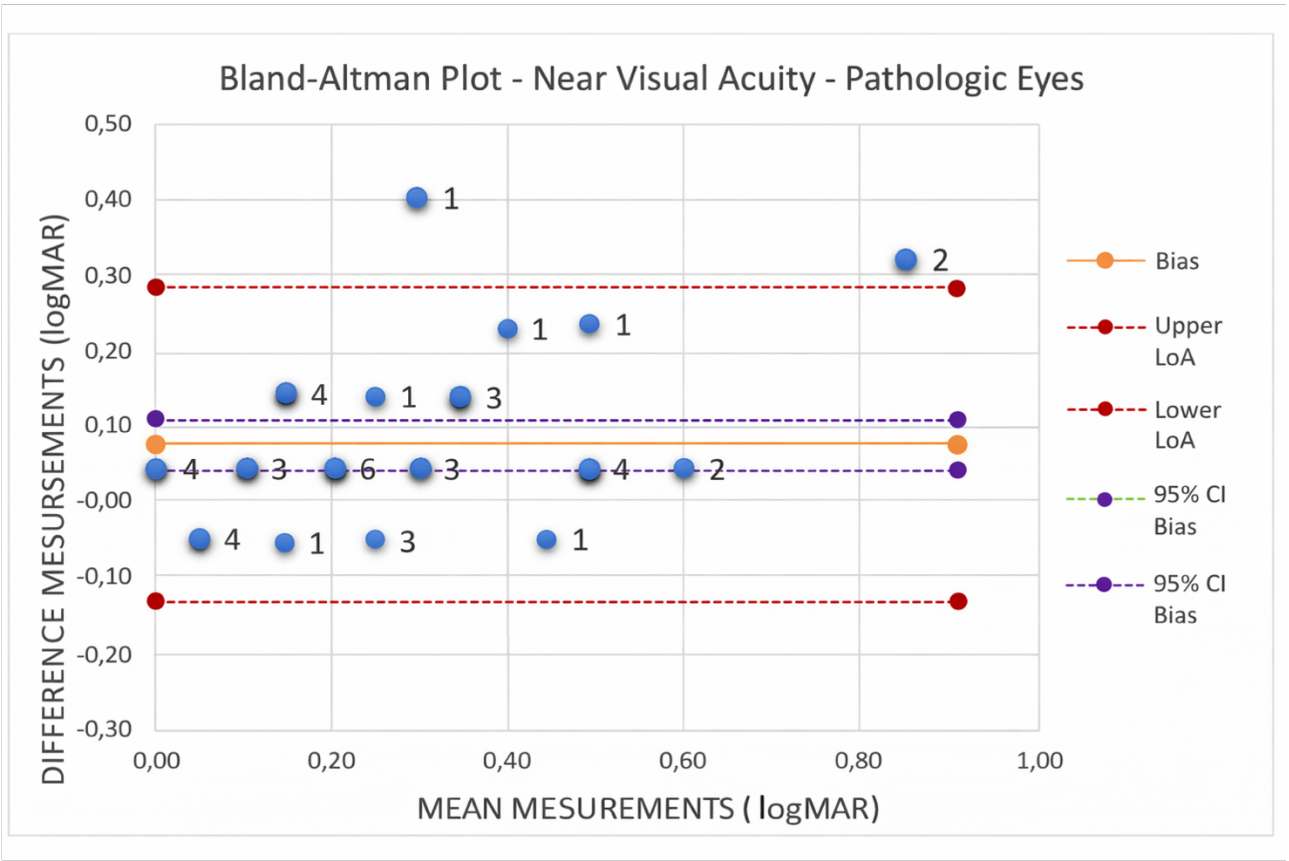

Figure 6 - In this Bland–Altman plot, the agreement between Smart Optometry and the Reduced Snellen near vision chart in measuring near visual acuity in pathologic eyes is evaluated. The bias line represents the mean difference between the two measurement methods. Upper LoA and Lower LoA correspond to the upper and lower limits of agreement, respectively. The two lines labeled as 95% CI of the bias represent the upper and lower bounds of the 95% confidence interval of the mean difference.

Amsler Grid Test

The Amsler test performed with Smart Optometry was positive in 27 eyes and negative in 71, whereas the paper grid was positive in 28 eyes and negative in 70 (Table 4). Cohen's kappa was 0.77, indicating substantial agreement. The same analysis was performed for healthy and diseased eye subgroups.

	Paper Grid – Positive	**Paper Grid – Negative**	**Total**
Smart Optometry – Positive	23	4	27
Smart Optometry – Negative	5	66	71
Total	28	70	98

Parameter	**Value**
Proportion of Agreement	0.91
Expected Frequency – Positives	7.71
Expected Frequency – Negatives	50.71
Chance Agreement Proportion	0.60
Cohen's Kappa	**0.77**

Table 4 - Results obtained from the analysis of the data collected for the Amsler grid test. Cohen's kappa was calculated including both healthy and pathologic eyes. The parameters derived from the cross-tabulation of the paper grid results and the smartphone-based grid results were used to compute Cohen's kappa coefficient.

In healthy eyes, the Smart Optometry Amsler test was positive in 6 and negative in 48; the paper grid was positive in 5 and negative in 49. Cohen's kappa was 0.90 (Table 5), indicating almost perfect agreement.

	Paper Grid – Positive	**Paper Grid – Negative**	**Total**
Smart Optometry – Positive	5	1	6
Smart Optometry – Negative	0	48	48
Total	5	49	54

Parameter	**Value**
Proportion of Agreement	0.98
Expected Frequency – Positives	0.56
Expected Frequency – Negatives	43.56
Chance Agreement Proportion	0.82
Cohen's Kappa	**0.90**

Table 5 - Results obtained from the analysis of the data collected for the Amsler grid test in healthy eyes.The parameters derived from the cross-tabulation of the paper grid results and the smartphone-based grid results were used to calculate Cohen's kappa coefficient.

In diseased eyes, Smart Optometry yielded 21 positives and 23 negatives; the paper grid yielded 23 positives and 21 negatives (Table 6). Cohen's kappa was 0.64, indicating substantial agreement.

	Paper Grid – Positive	**Paper Grid – Negative**	**Total**
Smart Optometry – Positive	18	3	21
Smart Optometry – Negative	5	18	23
Total	23	21	44

Parameter	**Value**
Proportion of Agreement	0.82
Expected Frequency – Positives	10.98
Expected Frequency – Negatives	10.98
Chance Agreement Proportion	0.50
Cohen's Kappa	**0.64**

Table 6 - Results obtained from the analysis of the data collected for the Amsler grid test in pathologic eyes.
The parameters derived from the cross-tabulation of the paper grid results and the smartphone-based grid results were used to calculate Cohen's kappa coefficient.

Discussion

Agreement of Peek Acuity Pro for distance visual acuity and Smart Optometry for near visual acuity—compared with ETDRS at 3 m and the Reduced Snellen near chart—was assessed using Bland–Altman analysis, focusing on:

- How close the mean difference is to zero (indicating whether app results match, overestimate, or underestimate in-person testing).
- Whether the equality line falls within the 95% CI of the bias (bias not statistically significant).
- The range of mean measurements (to verify consistency across healthy vs diseased eyes).
- The standard error (bias), used to judge interchangeability; in this study, clinical acceptability was set at 0.04 logMAR.

Distance Visual Acuity

Overall, Peek Acuity Pro slightly overestimated distance visual acuity compared with the 3-m ETDRS chart. The bias was not statistically significant because the mean difference was −0.02 logMAR and the equality line lay within the 95% CI. Since the average error corresponded to one letter, the two systems show high agreement.

In healthy eyes, Peek Acuity Pro again slightly overestimated acuity, with a mean difference of −0.01 logMAR and non-significant bias. The range of values was consistent with ETDRS, with a tendency toward slightly better acuity values. The average error was less than one letter, indicating excellent agreement.
In diseased eyes, Peek Acuity Pro results were slightly overestimated (mean difference −0.03 logMAR) with non-significant bias. Values were consistent with the chart-based measurements. The average error corresponded to about one and a half letters, again indicating strong agreement.
Overall, Peek Acuity Pro shows excellent agreement with the ETDRS chart at 3 meters, with slightly closer agreement in healthy than diseased eyes (mean differences −0.01 vs −0.03 logMAR).

Existing literature comparing Peek Acuity Pro to in-person systems aligns with these findings. A sensitivity/specificity study in pediatric screening reported a slight tendency toward overestimation and high specificity for identifying visual deficits[65] . Zhao et al. (2019) reported high intraclass correlation between Peek Acuity Pro and Snellen optotypes in a pediatric population; however, ICC assesses correlation rather than interchangeability and does not quantify measurement overlap [66]. In 2022, Bhaskaran et al. compared Peek Acuity Pro with Snellen charts and found high agreement across subgroups; notably, severe ocular pathologies were excluded in that study, whereas macular diseases were included in ours[67]. Compared with Peek Acuity Pro validation studies, the inclusion of patients with significant macular disorders in our cohort broadens the spectrum of clinical contexts in which this test has been evaluated.

Near Visual Acuity

From the overall analysis, Smart Optometry produced neither under- nor overestimation compared with the Reduced Snellen near chart, as the mean difference was 0.0 logMAR and the equality line overlapped the bias line. With a standard error equivalent to zero letters, the two systems demonstrate excellent agreement.

In healthy eyes, Smart Optometry slightly overestimated acuity (mean difference −0.03 logMAR). The bias was statistically significant because the equality line lay outside the 95% CI. This finding may be attributable to the relatively small number of samples. The range of values was comparable to the paper chart, with a tendency toward slightly worse acuity. The standard error corresponded to one and a half letters, suggesting practical interchangeability.

In diseased eyes, Smart Optometry slightly underestimated acuity (mean difference 0.03 logMAR), with non-significant bias. Again, the range of values was similar, and Smart Optometry tended to yield slightly better acuity values.

The standard error corresponded to one and a half letters, suggesting practical interchangeability.

To date, no prior studies have specifically evaluated Smart Optometry against standard near charts. In our study, the application showed high agreement with paper-based near acuity testing. Similar findings have been reported with other near-vision apps using comparable mechanisms[68,69] whereas other studies comparing near-vision apps to ETDRS or Snellen charts reported lower agreement [70].

Amsler Grid

Agreement between the digital and paper Amsler grid was assessed using Cohen's kappa. Considering all eyes, agreement was substantial (K in the 0.61–0.80 range per Landis and Koch).
In healthy eyes, agreement was almost perfect (K > 0.80). In diseased eyes, agreement remained substantial, though closer to the lower end of the "substantial" range.
Thus, the digital Amsler grid in Smart Optometry provides results similar to the paper Amsler grid, particularly in healthy eyes, with slightly reduced agreement in eyes affected by macular disease.

Several factors may influence smartphone-based testing. One is device resolution[71]: differences in performance between studies may reflect screen pixelation and optotype distortion. Another is screen brightness: during data collection—especially with Peek Acuity Pro at 100% brightness—it was sometimes necessary to reduce brightness by approximately 20% because some patients reported difficulty reading. Excessive ambient illumination can also cause screen reflections and impair readability[63]. Finally, distance visual acuity values may differ slightly due to the use of different optotypes (tumbling E vs ETDRS letters), although some studies have not found major differences between charts [72].

Conclusions

The results of this pilot study confirm findings reported in the literature and allow new observations. The patterns emerging from the collected data—particularly regarding healthy versus diseased eyes—should be further investigated in a larger, prospective study enabling test–retest assessment.
Smart Optometry and Peek Acuity Pro allow near visual acuity testing, distance visual acuity testing, and the Amsler grid test to be performed in a manner comparable to methods routinely used in outpatient clinics. Moreover, based on our analyses, app-derived measurements are sufficiently concordant with standard methods. The reliability of results obtained with Peek Acuity Pro and Smart Optometry suggests that these tools could be considered for a future telemedicine service. This could enable many patients—most of whom are elderly—to perform ophthalmic psychophysical tests at home, reducing the need to travel to central facilities.
Although many elderly patients cannot use smartphones or computers, during data collection some patients spontaneously expressed support for the idea of a future telemedicine service. A telemedicine program using Smart Optometry and Peek Acuity Pro could be accessible to a broad population, including individuals who are illiterate or affected by aphasia, because both apps can use tumbling “E” optotypes.

Limitations

Limitation of this study is the lack of test–retest repeatability assessment in the same subjects. If performed, limits of agreement could be estimated more precisely, and the reliability of the findings would be strengthened.

Future perspectives

In the future, teleophthalmology may improve proximity medicine services by extending access to testing for a large number of individuals, including those

living far from hospitals, those with motor impairment, and those living in rural areas.

The encouraging results of this study—reinforcing an increasing body of scientific evidence—suggest a near future in which telemedicine is implemented in ophthalmology and successfully integrated into everyday clinical practice.

General Conclusions

Integrated interpretation of the thesis findings

The present thesis was designed to investigate macular diseases through three interconnected levels of analysis: molecular regulation, retinal microstructure, and functional monitoring. Although each chapter addresses a distinct experimental or clinical question, the overall contribution of the thesis lies in the integration of these levels into a unified translational model.
The first chapter demonstrated that human Müller cell-derived MIO-M1 cultures respond to subthreshold 520 nm laser stimulation through measurable transcriptional modulation. The observed changes involved genes related to ion transport, solute handling, extracellular matrix organization, vascular signaling, glial activation, and redox regulation, without evidence of a coordinated activation of canonical apoptotic or necrotic pathways. These findings suggest that subthreshold laser stimulation may induce regulated cellular adaptation rather than destructive injury. However, these data should be interpreted as mechanistic and hypothesis-generating, since transcriptomic modulation does not directly prove functional improvement in retinal fluid transport or therapeutic efficacy in vivo.

The second chapter translated this biological rationale into a clinical imaging setting by evaluating Müller cell-related OCT biomarkers in macular edema secondary to retinal vein occlusion. The preservation or alteration of the Müller cell cone, together with the integrity of the ELM and IZ/EZ complex and changes in central retinal thickness, provided structural information on retinal organization after anti-VEGF therapy. The findings suggest that eyes with preserved Müller cell cone architecture may show a more favorable anatomical response and greater maintenance of outer retinal integrity. Nevertheless, the relationship between structural preservation and visual improvement appears multifactorial, and the results should be interpreted within the limits of a retrospective design and a relatively small subgroup of Müller cell cone-altered eyes.

The third chapter extended this integrated framework toward clinical applicability by assessing smartphone-based tools for functional evaluation in patients with macular disease. Digital visual acuity testing and Amsler grid assessment may provide a practical method for repeated functional monitoring, particularly in chronic retinal conditions requiring long-term follow-up. These tools are not intended to replace OCT imaging or specialist examination but may complement them by adding an accessible functional layer to disease monitoring.

Taken together, the thesis supports a model in which macular disease assessment should move beyond isolated anatomical or functional parameters. Müller cells may represent a biological link between molecular response, structural stability, and functional evolution. OCT biomarkers provide a clinically accessible representation of retinal microstructural integrity, while digital functional testing may allow longitudinal monitoring of visual performance in real-world settings. The integration of these approaches may contribute to more personalized diagnostic and therapeutic pathways in retinal diseases.

The original contribution of this thesis is therefore threefold. First, it provides novel transcriptomic data on the response of Müller cells to subthreshold green laser stimulation, an area that remains underexplored compared with retinal pigment epithelium-centered studies. Second, it applies the concept of Müller cell-related structural integrity to RVO-associated macular edema, focusing on the Müller cell cone as a clinically relevant OCT biomarker. Third, it evaluates digital functional testing as a potential component of telemedicine-based monitoring in macular disease. By linking these three domains, the thesis proposes a translational pathway from cellular biology to retinal imaging and finally to patient-centered clinical monitoring.

Bibliography

1. Chang DB, Luttrull JK. Comparison of Subthreshold 577 and 810 nm Micropulse Laser Effects on Heat-Shock Protein Activation Kinetics: Implications for Treatment Efficacy and Safety. *Transl Vis Sci Technol*. 2020;9(5):1-8. doi:10.1167/TVST.9.5.23
2. Inagaki K, Shuo T, Katakura K, Ebihara N, Murakami A, Ohkoshi K. Sublethal Photothermal Stimulation with a Micropulse Laser Induces Heat Shock Protein Expression in ARPE-19 Cells. *J Ophthalmol*. 2015;2015(1):729792. doi:10.1155/2015/729792
3. Shiraya T, Araki F, Nakagawa S, et al. Differential gene expression analysis using RNA sequencing: retinal pigment epithelial cells after exposure to continuous-wave and subthreshold micropulse laser. *Jpn J Ophthalmol*. 2022;66(5):487-497. doi:10.1007/S10384-022-00925-0
4. Yan W, Peng YR, van Zyl T, et al. Cell Atlas of The Human Fovea and Peripheral Retina. *Sci Rep*. 2020;10(1). doi:10.1038/S41598-020-66092-9
5. Franze K, Grosche J, Skatchkov SN, et al. Muller cells are living optical fibers in the vertebrate retina. *Proc Natl Acad Sci U S A*. 2007;104(20):8287-8292. doi:10.1073/PNAS.0611180104
6. Agte S, Junek S, Matthias S, et al. Müller Glial Cell-Provided Cellular Light Guidance through the Vital Guinea-Pig Retina. *Biophys J*. 2011;101(11):2611-2619. doi:10.1016/J.BPJ.2011.09.062
7. Labin AM, Safuri SK, Ribak EN, Perlman I. Müller cells separate between wavelengths to improve day vision with minimal effect upon night vision. *Nat Commun*. 2014;5. doi:10.1038/NCOMMS5319
8. Lindenau W, Kuhrt H, Ulbricht E, Körner K, Bringmann A, Reichenbach A. Cone-to-Müller cell ratio in the mammalian retina: A survey of seven mammals with different lifestyle. *Exp Eye Res*. 2019;181:38-48. doi:10.1016/j.exer.2019.01.012
9. Midena E, Bini S, Martini F, et al. CHANGES OF AQUEOUS HUMOR MÜLLER CELLS' BIOMARKERS IN HUMAN PATIENTS AFFECTED BY DIABETIC MACULAR EDEMA AFTER SUBTHRESHOLD MICROPULSE LASER TREATMENT. *Retina*. 2020;40(1):126-134. doi:10.1097/IAE.0000000000002356
10. Midena E, Micera A, Frizziero L, Pilotto E, Esposito G, Bini S. Sub-threshold micropulse laser treatment reduces inflammatory biomarkers in aqueous humour of diabetic patients with macular edema. *Sci Rep*. 2019;9(1). doi:10.1038/S41598-019-46515-Y
11. Limb GA, Salt TE, Munro PMG, Moss SE, Khaw PT. *In Vitro Characterization of a Spontaneously Immortalized Human Müller Cell Line (MIO-M1)*.
12. Dobin A, Davis CA, Schlesinger F, et al. STAR: ultrafast universal RNA-seq aligner. *Bioinformatics*. 2013;29(1):15-21. doi:10.1093/BIOINFORMATICS/BTS635
13. Liao Y, Smyth GK, Shi W. featureCounts: an efficient general purpose program for assigning sequence reads to genomic features.

Bioinformatics. 2014;30(7):923-930. doi:10.1093/BIOINFORMATICS/BTT656
14. Robinson MD, McCarthy DJ, Smyth GK. edgeR: a Bioconductor package for differential expression analysis of digital gene expression data. *Bioinformatics*. 2010;26(1):139-140. doi:10.1093/BIOINFORMATICS/BTP616
15. Leek JT, Johnson WE, Parker HS, Jaffe AE, Storey JD. The sva package for removing batch effects and other unwanted variation in high-throughput experiments. *Bioinformatics*. 2012;28(6):882. doi:10.1093/BIOINFORMATICS/BTS034
16. Smyth GK, Ritchie ME, Law CW, et al. RNA-seq analysis is easy as 1-2-3 with limma, Glimma and edgeR. *F1000Res*. 2018;5:ISCB Comm J-1408. doi:10.12688/F1000RESEARCH.9005.3
17. Kassambara A, Mundt F. Extract and Visualize the Results of Multivariate Data Analyses [R package factoextra version 1.0.7]. *CRAN: Contributed Packages*. Published online April 1, 2020. doi:10.32614/CRAN.PACKAGE.FACTOEXTRA
18. Gu Z. Complex heatmap visualization. *iMeta*. 2022;1(3):e43. doi:10.1002/IMT2.43
19. Lê S, Josse J, Husson F. FactoMineR: An R Package for Multivariate Analysis. *J Stat Softw*. 2008;25(1):1-18. doi:10.18637/JSS.V025.I01
20. CRAN: Package factoextra. Accessed February 27, 2026. https://cran.r-project.org/web/packages/factoextra/index.html
21. Barber AJ, Lieth E, Khin SA, Antonetti DA, Buchanan AG, Gardner TW. Neural apoptosis in the retina during experimental and human diabetes. Early onset and effect of insulin. *J Clin Invest*. 1998;102(4):783-791. doi:10.1172/JCI2425
22. Lavinsky D, Sramek C, Wang J, et al. Subvisible retinal laser therapy: Titration algorithm and tissue response. *Retina*. 2014;34(1):87-97. doi:10.1097/IAE.0B013E3182993EDC
23. Lavinsky D, Wang J, Huie P, et al. Nondamaging Retinal Laser Therapy: Rationale and Applications to the Macula. *Invest Ophthalmol Vis Sci*. 2016;57(6):2488. doi:10.1167/IOVS.15-18981
24. Vujosevic S, Frizziero L, Martini F, et al. Single retinal layer changes after subthreshold micropulse yellow laser in diabetic macular edema. *Ophthalmic Surg Lasers Imaging Retina*. 2018;49(11):E218-E225. doi:10.3928/23258160-20181101-22
25. Gao H, A L, Huang X, Chen X, Xu H. Müller Glia-Mediated Retinal Regeneration. *Mol Neurobiol. Springer*. 2021;58(5):2342-2361. doi:10.1007/s12035-020-02274-w
26. Hollborn M, Tenckhoff S, Jahn K, et al. Changes in retinal gene expression in proliferative vitreoretinopathy: glial cell expression of HB-EGF. *Mol Vis*. 2005;11:397-413.
27. Reichenbach A, Bringmann A. New functions of Müller cells. *Glia*. 2013;61(5):651-678. doi:10.1002/GLIA.22477
28. Kofuji P, Biedermann B, Siddharthan V, et al. Kir potassium channel subunit expression in retinal glial cells: implications for spatial potassium buffering. *Glia*. 2002;39(3):292-303. doi:10.1002/GLIA.10112
29. Liu X. SLC Family Transporters. *Adv Exp Med Biol*. 2019;1141:101-202. doi:10.1007/978-981-13-7647-4_3

30. Sher A, Jones BW, Huie P, et al. Restoration of Retinal Structure and Function after Selective Photocoagulation. *The Journal of Neuroscience*. 2013;33(16):6800. doi:10.1523/JNEUROSCI.1044-12.2013
31. Tonelli C, Chio IIC, Tuveson DA. Transcriptional Regulation by Nrf2. *Antioxid Redox Signal*. 2018;29(17):1727-1745. doi:10.1089/ARS.2017.7342
32. Marengo B, Nitti M, Furfaro AL, et al. Redox Homeostasis and Cellular Antioxidant Systems: Crucial Players in Cancer Growth and Therapy. *Oxid Med Cell Longev*. 2016;2016. doi:10.1155/2016/6235641
33. Song P, Xu Y, Zha M, Zhang Y, Rudan I. Global epidemiology of retinal vein occlusion: a systematic review and meta-analysis of prevalence, incidence, and risk factors. Published online 2019. doi:10.7189/jogh.09.010427
34. Tsang K, Hui V, Pang C, et al. SD-OCT-based biomarkers in predicting treatment outcomes of macular oedema secondary to retinal vein occlusion treated with anti-VEGF therapy. *Acta Ophthalmol*. Published online 2025. doi:10.1111/aos.17574
35. Tao Y, Ge L, Su N, et al. Exploration on OCT biomarker candidate related to macular edema caused by diabetic retinopathy and retinal vein occlusion in SD-OCT images. *Sci Rep*. 2024;14. doi:10.1038/s41598-024-63144-2
36. Munk M, Ceklic L, Stillenmunkes R, et al. Integrated Assessment of OCT, Multimodal Imaging, and Cytokine Markers for Predicting Treatment Responses in Retinal Vein Occlusion Associated Macular Edema: A Comparative Review of Anti-VEGF and Steroid Therapies. *Diagnostics*. 2024;14. doi:10.3390/diagnostics14171983
37. Ali AOM, Saleh SY, Mohammed AESAA, Saleh M. Correlation between Visual Acuity and Optical Coherence Tomography Biomarkers in Retinal Vein Occlusion. *Egyptian Retina Journal*. Published online 2024. doi:10.4103/erj.erj_4_23
38. Sekerinov D, Shekerinov N, Dimovska VJ, Petrushevska A. EVALUATION BIOMARKERS ON OPTICAL COHERENCE TOMOGRAPHY IN PATIENTS WITH MACULAR EDEMA DUE TO CENTRAL RETINAL VEIN OCCLUSION WITH ANTIANGIOGENE TREATMENT. *Journal of Morphological Sciences*. Published online 2025. doi:10.55302/jms2581131s
39. Viggiano P, Bisceglia G, Bacherini D, et al. LONG-TERM VISUAL OUTCOMES AND OPTICAL COHERENCE TOMOGRAPHY BIOMARKERS IN EYES WITH MACULAR EDEMA SECONDARY TO RETINAL VEIN OCCLUSION FOLLOWING ANTI-VASCULAR ENDOTHELIAL GROWTH FACTOR THERAPY. *Retina*. 2024;44:1572-1579. doi:10.1097/iae.0000000000004157
40. Castro-Navarro V, Monferrer-Adsuara C, Navarro-Palop C, Montero-Hernández J, Cervera-Taulet E. Optical coherence tomography biomarkers in patients with macular edema secondary to retinal vein occlusion treated with dexamethasone implant. *BMC Ophthalmol*. 2021;22. doi:10.1186/s12886-022-02415-w
41. Siedlecki J, Hattenbach L, Feltgen N, Priglinger S. Biomarker in der Therapie venöser retinaler Gefäßverschlüsse. *Die Ophthalmologie*. 2022;119:1111-1120. doi:10.1007/s00347-022-01732-1
42. Yiu G, Welch J, Wang Y, Wang Z, Wang PW, Haskova Z. Spectral-Domain OCT Predictors of Visual Outcomes after Ranibizumab Treatment for

Macular Edema Resulting from Retinal Vein Occlusion. *Ophthalmol Retina*. Published online 2019. doi:10.1016/j.oret.2019.08.009
43. Ding X, Hu Y, Yu H, Li Q. Changes of Optical Coherence Tomography Biomarkers in Macular Edema Secondary to Retinal Vein Occlusion After Anti-VEGF and Anti-Inflammatory Therapies. *Drug Des Devel Ther*. 2022;16:717-725. doi:10.2147/dddt.s351683
44. Hatamnejad A, Nanji K, Grad J, et al. Predicting Treatment Response in Retinal Vein Occlusions Using Baseline Optical Coherence Tomography Biomarkers: A Systematic Review. *Surv Ophthalmol*. Published online 2025. doi:10.1016/j.survophthal.2025.08.016
45. Arrigo A, Aragona E, Antropoli A, et al. Foveal Eversion is Associated with High Persistence of Macular Edema and Visual Acuity Deterioration in Retinal Vein Occlusion. *Ophthalmol Ther*. 2023;12:2157-2169. doi:10.1007/s40123-023-00734-9
46. Hirano Y, Suzuki N, Tomiyasu T, et al. Multimodal Imaging of Microvascular Abnormalities in Retinal Vein Occlusion. *J Clin Med*. 2021;10. doi:10.3390/jcm10030405
47. Midena E, Torresin T, Schiavon S, et al. The Disorganization of Retinal Inner Layers Is Correlated to Müller Cells Impairment in Diabetic Macular Edema: An Imaging and Omics Study. *Int J Mol Sci*. 2023;24. doi:10.3390/ijms24119607
48. Silitonga A, Silitonga H, Virgana R, et al. Prognostics optical coherence tomography biomarker in macular oedema secondary to retinal vein occlusion. *African Vision and Eye Health*. Published online 2025. doi:10.4102/aveh.v84i1.965
49. Danilova E, Plokhih I, Dzhanbekova L, et al. Microcystic Macular Edema: Clinical Significance and Pathogenetic Mechanisms. *Journal of Clinical Practice*. Published online 2025. doi:10.17816/clinpract680846
50. Desideri L, Kojima K, Eldridge N, et al. Integration of Proteomics and Artificial Intelligence-Driven OCT Biomarker Analysis in Central Vein Retinal Occlusion. *Exp Eye Res*. Published online 2025:110462. doi:10.1016/j.exer.2025.110462
51. Zeng Y, Zhang X, Mi L, et al. Characterization of Macrophage-Like Cells in Retinal Vein Occlusion Using En Face Optical Coherence Tomography. *Front Immunol*. 2022;13. doi:10.3389/fimmu.2022.855466
52. Wang W, Sun G, He L, Chen C. Increased Macrophage-like Cell Density in Retinal Vein Occlusion as Characterized by en Face Optical Coherence Tomography. *J Clin Med*. 2022;11. doi:10.3390/jcm11195636
53. Gass JDM. Müller cell cone, an overlooked part of the anatomy of the fovea centralis: hypotheses concerning its role in the pathogenesis of macular hole and foveomacualr retinoschisis. *Arch Ophthalmol*. 1999;117(6):821-823. doi:10.1001/ARCHOPHT.117.6.821
54. Choi M, Yun C, Oh JH, Kim SW. FOVEAL MÜLLER CELL CONE AS A PROGNOSTIC OPTICAL COHERENCE TOMOGRAPHY BIOMARKER FOR INITIAL RESPONSE TO ANTIVASCULAR ENDOTHELIAL GROWTH FACTOR TREATMENT IN CYSTOID DIABETIC MACULAR EDEMA. *Retina*. 2022;42(1):129-137. doi:10.1097/IAE.0000000000003271
55. Arrigo A, Aragona E, Capone L, Lattanzio R, Zollet P, Bandello F. Foveal Eversion: A Possible Biomarker of Persistent Diabetic Macular Edema. *Ophthalmol Ther*. 2021;10(1):115-126. doi:10.1007/S40123-020-00324-Z

56. Kawaguchi A, Sharafeldin N, Sundaram A, et al. Tele-Ophthalmology for Age-Related Macular Degeneration and Diabetic Retinopathy Screening: A Systematic Review and Meta-Analysis. *Telemed J E Health*. 2018;24(4):301-308. doi:10.1089/TMJ.2017.0100
57. Weng CY, Maguire MG, Flaxel CJ, et al. Effectiveness of Conventional Digital Fundus Photography-Based Teleretinal Screening for Diabetic Retinopathy and Diabetic Macular Edema: A Report by the American Academy of Ophthalmology. *Ophthalmology*. 2024;131(8):927-942. doi:10.1016/J.OPHTHA.2024.02.017
58. Sharafeldin N, Kawaguchi A, Sundaram A, et al. Review of economic evaluations of teleophthalmology as a screening strategy for chronic eye disease in adults. *Br J Ophthalmol*. 2018;102(11):1485-1491. doi:10.1136/BJOPHTHALMOL-2017-311452
59. Keenan J, Shahid H, Bourne RR, White AJ, Martin KR. Cambridge community Optometry Glaucoma Scheme. *Clin Exp Ophthalmol*. 2015;43(3):221-227. doi:10.1111/CEO.12398
60. Kiage D, Kherani IN, Gichuhi S, Damji KF, Nyenze M. The Muranga Teleophthalmology Study: Comparison of Virtual (Teleglaucoma) with in-Person Clinical Assessment to Diagnose Glaucoma. *Middle East Afr J Ophthalmol*. 2013;20(2):150-157. doi:10.4103/0974-9233.110604
61. Chew EY, Clemons TE, Bressler SB, et al. Randomized trial of a home monitoring system for early detection of choroidal neovascularization home monitoring of the Eye (HOME) study. *Ophthalmology*. 2014;121(2):535-544. doi:10.1016/J.OPHTHA.2013.10.027
62. Chew EY, Clemons TE, Bressler SB, et al. Randomized trial of the ForeseeHome monitoring device for early detection of neovascular age-related macular degeneration. The HOme Monitoring of the Eye (HOME) study design - HOME Study report number 1. *Contemp Clin Trials*. 2014;37(2):294-300. doi:10.1016/J.CCT.2014.02.003
63. Bastawrous A, Rono HK, Livingstone IAT, et al. Development and Validation of a Smartphone-Based Visual Acuity Test (Peek Acuity) for Clinical Practice and Community-Based Fieldwork. *JAMA Ophthalmol*. 2015;133(8):930-937. doi:10.1001/JAMAOPHTHALMOL.2015.1468
64. Satgunam PN, Thakur M, Sachdeva V, Reddy S, Rani PK. Validation of visual acuity applications for teleophthalmology during COVID-19. *Indian J Ophthalmol*. 2021;69(2):385-390. doi:10.4103/IJO.IJO_2333_20
65. de Venecia B, Bradfield Y, Trane RM, Bareiro A, Scalamogna M. Validation of Peek Acuity application in pediatric screening programs in Paraguay. *Int J Ophthalmol*. 2018;11(8):1384-1389. doi:10.18240/IJO.2018.08.21
66. Zhao L, Stinnett SS, Prakalapakorn SG. Visual Acuity Assessment and Vision Screening Using a Novel Smartphone Application. *J Pediatr*. 2019;213:203-210.e1. doi:10.1016/J.JPEDS.2019.06.021
67. Bhaskaran A, Babu M, Abhilash B, Sudhakar N, Dixitha V. Comparison of smartphone application-based visual acuity with traditional visual acuity chart for use in tele-ophthalmology. *Taiwan J Ophthalmol*. 2022;12(2):155-163. doi:10.4103/TJO.TJO_7_22
68. Han X, Scheetz J, Keel S, et al. Development and Validation of a Smartphone-Based Visual Acuity Test (Vision at Home). *Transl Vis Sci Technol*. 2019;8(4). doi:10.1167/TVST.8.4.27

69. Kim DG, Webel AD, Blumenkranz MS, et al. A Smartphone-Based Near-Vision Testing System: Design, Accuracy, and Reproducibility Compared With Standard Clinical Measures. *Ophthalmic Surg Lasers Imaging Retina*. 2022;53(2):79-84. doi:10.3928/23258160-20220121-05
70. Steren BJ, Young B, Chow J. Visual Acuity Testing for Telehealth Using Mobile Applications. *JAMA Ophthalmol*. 2021;139(3):344-347. doi:10.1001/JAMAOPHTHALMOL.2020.6177
71. Carkeet A, Lister LJ. Computer monitor pixellation and Sloan letter visual acuity measurement. *Ophthalmic and Physiological Optics*. 2018;38(2):144-151. doi:10.1111/opo.12434
72. Plainis S, Kontadakis G, Feloni E, et al. Comparison of Visual Acuity Charts in Young Adults and Patients with Diabetic Retinopathy. *Optometry and Vision Science*. 2013;90(2):174-178. doi:10.1097/OPX.0b013e31827ce251